THE INFLUENCE OF HYDROGEN CONTENT ON THERMO-MECHANICAL

PROPERTIES OF NICKEL-ALUMINUM

A Thesis

by

UGUR ASLAN

Submitted to the Office of Graduate and Professional Studies of
Texas A&M University
in partial fulfillment of the requirements for the degree of

MASTER OF SCIENCE

Chair of Committee,	Tahir Cagin
Committee Members,	Xiaofeng Qian
	Lin Shao
Head of Department,	Ibrahim Karaman

August 2017

Major Subject: Materials Science and Engineering

ABSTRACT

The effect of hydrogen on thermo-mechanical properties and in-use performance of metals and metal alloys is of critical importance, in particular in structural applications. In recent years, the relevance of H-metal interactions and their influence on expected performance have been broadened into functional metallic compounds and alloys as they are being used in energy, health and catalysis applications. In this work, we focused on NiAl compounds and shape memory alloys to assess the influence of H on thermal, physical, chemical, and mechanical properties using molecular dynamics (MD) and density functional theory (DFT) methods. The following alloys, Ni_3Al, Al_3Ni, NiAl, have been studied with H-content varied from 1% to 10% by MD at temperatures from 0 ^{o}K to 2100 ^{o}K for single crystals in B1, B2, L10, A4 structures and random and ordered L12 alloys. Furthermore, we studied specific bi-crystals with CSL grain boundaries: for B2 Σ 5(210), Σ 5(310), and Σ 3(210); for L10 Σ 5(210), Σ 5(310), Σ 3(210) to establish enthalpy-temperature concentration, volume-temperature concentration, volume-pressure-concentration relationships from which thermodynamic and mechanical response coefficients such as specific heats, thermal expansion, bulk modulus and isothermal compressibility and isothermal tensile and compression moduli and young moduli were determined by applying appropriate mechanical stresses.

ACKNOWLEDGEMENTS

CONTRIBUTORS AND FUNDING SOURCES

Contributors

The work presented in this Master of Science thesis is conducted and completed by the student, Ugur Aslan. The work was supervised by the thesis committee chair, Professor Tahir Cagin of the Department of Materials Science and Engineering, and guided further by the thesis committee members, Assistant Professor Xiaofeng Qian of the Department of Materials Science and Engineering and Associate Professor Lin Shao of the Department of Nuclear Engineering of Texas A&M University..

Funding Sources

TABLE OF CONTENTS

LIST OF FIGURES

LIST OF TABLES

1. INTRODUCTION

1.1   Hydrogen in metals and hydrogen metal interactions

Affinity of hydrogen to metals has been both a blessing and a curse depending on the engineering applications of metals and alloys. For instance, formation of many metal hydrides has been utilized for hydrogen storage applications or observations of a very strong tendency of hydrogen absorption capacity in some metals, e.g. in palladium, led to it in many industrial applications; such as its use in hydrogen storage or extracting hydrogen by cleansing or removing through the palladium membranes [1, 2]. In turn, the absorption of hydrogen has strongly changed the physical properties of the Pd such as brittleness, hardness, specific heat, resistivity, susceptibility etc. [3, 4]. This influence even included inducing phase transformation in Pd-hydrogen and other metal-hydrogen systems because the absorbed hydrogen atoms in metals distort the interstitial sites of the lattice and due to emergence of long-range strain fields. Hence due to these and other effects of hydrogen on thermo-mechanical, chemical, physical properties of metals, especially for structural metals, such as steels and alike the hydrogen metal-metal alloy interactions emerged as very active areas of research such as ultra-high vacuum [5, 6]. Examples include H-storage as it relates to fuel cell applications. In recent past two to three decades, the interest in hydrogen-metal interactions and their influence on expected performance of metals and metal alloys have been broadened as they appear in energy, health, catalysis, and functional applications of metals and metallic alloys and

compounds [7]. A very critical hydrogen-metal interaction problem is the hydrogen embrittlement effects in metals. Discussions on hydrogen embrittlement effects besides absorption of hydrogen first emerged as of late 19th century. Over the years extensive research efforts have been put forth in characterizing and development of an understanding of the mechanisms involved in this phenomenon. Hydrogen systems with alloys possess ionic, covalent and metallic bonds the most important one is metallic bonds among them. Sieverts discovered that the hydrogen concentration of the system is related to the pressure of hydrogen in minuscule levels [1]. Over the last a few decades, hydrogen metals systems have been investigated with the help of computational studies to find out the detailed description of microscopic level behavior of hydrogen in the H-metal systems, these may include the structural, thermodynamic (e.g., solubility), mechanical and dynamic-transport properties [8]. The conception of hydrogen is pivotal to solve the unexpected hazardous effects of hydrogen in metal systems and be able to oppose the harmful effects adversely to help keep storing energy and fabricating interest of energy amounts in applications [8].

The real hydrogen amount in metals varies according to the equilibrium value due to the absorption or the opposite process of absorption that is desorption which generally hindered or facilitated on the surfaces of metals. This phenomenon is crucial on applications to electronic systems [9, 10]. Once hydrogen enters into metals the hydrogen atoms which are absorbed separated from interstitial areas in bulk metal and the hydrogen atoms in metals migrate among interstitial neighboring locations which results in tremendously great diffusion rate even at low temperatures [11, 12]. Since the

hydrogen is the lightest element, quantum effects become critical in H-diffusivity. Moreover hydrogen atoms in the interstitials sites alter the properties of the metals significantly e.g. thermo-mechanical, dynamical, electronic or even magnetic. As a result of this, the phonon spectrum undergoes the small changes and as well which leads systems into complex phase diagrams due to the hydrogen content and facile diffusion [13] processes affecting the structure even at low temperatures (under 25 $^\circ$C).

1.2 NiAl alloys and hydrogen

NiAl is a very common intermetallic compound of aluminum and nickel. It has a large number of uses in industries such as aerospace, marine, oil and gas etc. In addition to that, NiAl alloys are shape memory alloys used particularly taking advantage of this property of the alloy in various technological applications [14, 15]. H-NiAl alloy-compound interactions, influence of its properties, deterioration of its properties due to interaction with hydrogen has not been explored in detail, although there are some recent interest, it still poses itself as a critical and fundamental materials science and engineering problem. The constituents in NiAl are nickel and aluminum. Nickel is a shiny metal and has a lustrous appearance. Nickel comes out hard and ductile among transition metals. On the other hand, aluminum is a silvery-gray metal and one of the most abundant metal in the earth. Some of the characteristics of Al are light, low-density [16], non-magnetic, ductile [17] etc.

NiAl has the B2 crystal structure which is one atom at the center and one eighth of the atom at the every corner in a cubic cell [18]. The compositional range in NiAl is

changing from 43% to 69% Ni. At 1400 °C and as the temperature decreases to 400 °C

the range goes down from 45% to 59% [18]. When we cool it down to the room

temperature slowly it ends up in one stable phase, B2 phase that has less Ni

concentration than the Ni of NiAl alloy at higher temperature, and one metastable phase,

L12 that has more Ni concentration than the concentration of Ni of NiAl alloy at higher

temperature. On the fast cooling process (Quenching), NiAl is subjected to the

thermoelastic martensitic transformation, crystal structure of which is L10 that is the

body centered tetragonal phase [18]. That martensitic NiAl shows shape memory effect

which means regaining its original shape through heating process after some extent to

plastic deformation. The point where the martensitic transformation starts has a

temperature value that is Ms approximately 900 °C, definitely depends on the Ni and Al

ratio [18]. The binary NiAl is, however, still quite brittle around the room temperature

due to its intrinsic properties.

It is known that hydrogen strongly affects the crack growth on grain boundaries of

metals in turn overall fracture behavior. Notwithstanding, the true intrinsic

characteristics of embrittlement process is still not totally solved on account of the

complicated interrelations of structure and chemistry of materials although there are

many theories trying to explain it. Hydrogen has become extremely popular on account

of active and solubility properties in metals for a few decades. Hydrogen may easily be

doped due to its mass, which is very light and small, which can land in vacancies,

interstitial sites, dislocations [19] etc. These phenomena degrade the perfection and

engineering performance of materials. The detailed studies on how the solvation

(absorption) of hydrogen interaction with the metal and interactions in the presence of defects (vacancy, dislocations, grain boundaries) can lead to a better understanding of these phenomena.

In this master thesis research, we use computational methods such as density functional theory and molecular dynamics to investigate the influence of H on the thermo-mechanical properties of H on NiAl alloys. Figure 1 was built by using VESTA [20]. I have constructed the models of B1, B2, L10, L12, A4 crystal structures of NiAl and bulk A1 crystal structure of Ni and Al separately for a single cell and I have used Vienna Ab initio Simulation Package (VASP) [21-23] and all the data in VASP obtained by the PAW potentials [24, 25]. The B1 structure has 8 atoms which are 4 aluminum and 4 nickel atoms and whose space group is Fm3m and the prototype structure of B1 is sometimes called NaCl shown in Figure 1 a. As well as its crystal system is cubic. The B2 crystal structure that possesses one nickel atom and one aluminum atom which is total 2 atoms and the space group of B2 crystal structure is Pm3m. In addition to that its prototype structure is called CsCl and have a cubic crystal system shown in Figure 1 b. The L10 structure has 4 atoms, two of which are aluminum and the other two are nickel atoms. Its space group number is P4/mmm and has a cubic system shown in Figure 1 c. The L12 structure has also 4 atoms which three of them belong to one type and the remaining one belongs to the other type. Its space group number is Pm3m and has a cubic crystal system shown in Figure 1 d. The A4 crystal structure has eight atoms, four of them are aluminum atoms and the other four are nickel atoms whose space group is Fd3m and is a member of the cubic crystal system demonstrated in Figure 1 e.
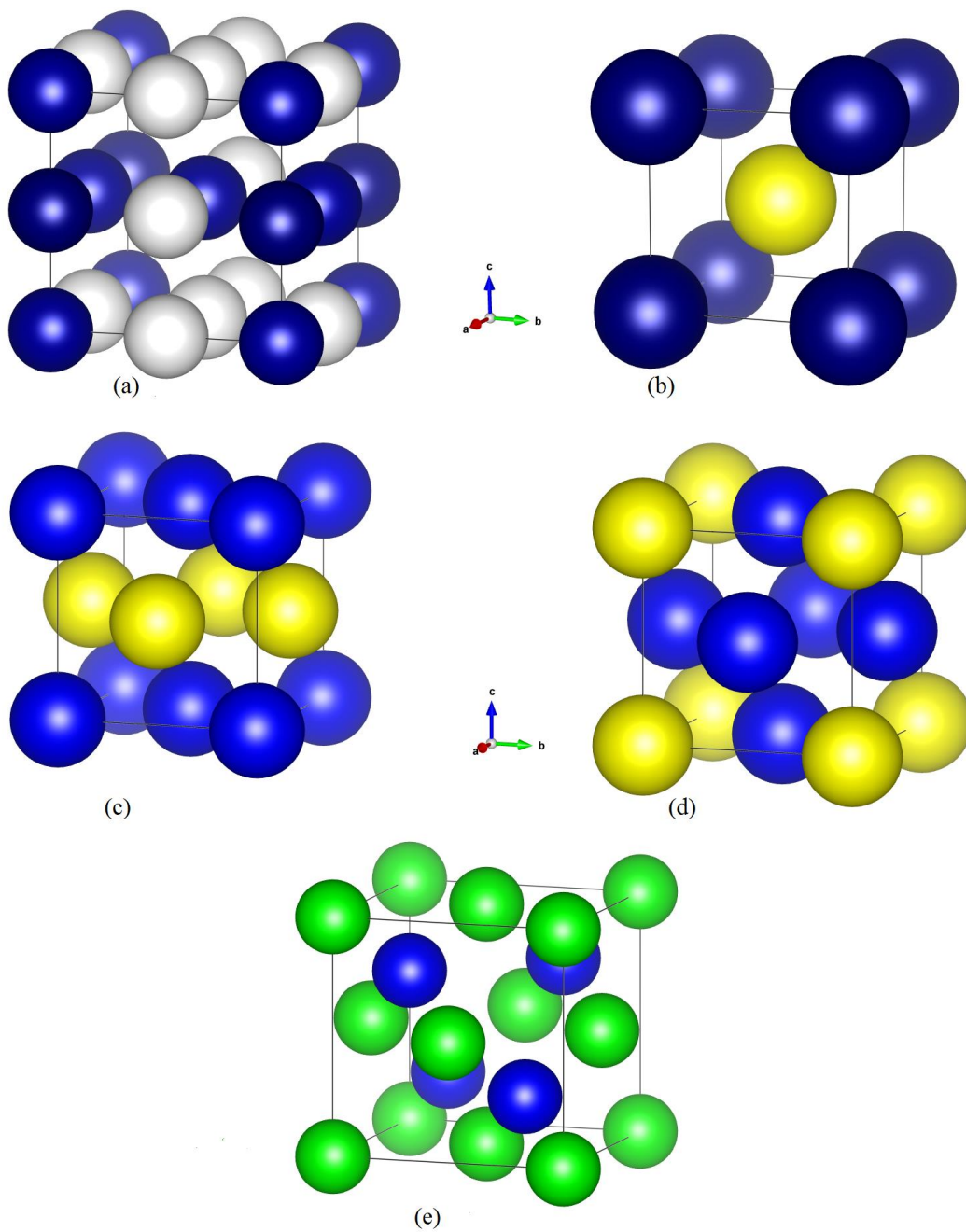
Figure 1: The prototype crystal structures of NiAl alloys used in DFT a) B1 NaCl structure b) B2 CsCl structure c) L10 AuCu structure d) L12 AuCu structure e) A4 diamond structure.

I also employed molecular dynamics simulations of NiAl structures in Large-scale Atomic/Molecular Massively Parallel Simulator (LAMMPS) [11], which is mostly used for conducting classical molecular dynamics. I have constructed the supercell model systems in B1, B2, and A1 of NiAl along with ordered and random L12 structures of the NiAl systems. I have studied H-content influence through introducing hydrogen to all the systems described above with hydrogen content ratios: 0.01, 0.02, 0.05, 0.08 and 0.1.

For studying bicrystal systems, I have constructed 6 different grain boundary structures which are A1 and B2 with 3 different grain boundary planes and orientations, they are B2 Σ 5(210), B2 Σ 5(310), B2 Σ 3(210) and L10 Σ 5(210), L10 Σ 5(310), L10 Σ 3(210). I have investigated the grain boundary effect in B2, A1 NiAl structures with $\Sigma = 3$ and $\Sigma = 5$ with different orientations that are (210) and (310) planes for both structures, the system sizes for these bicrystals are 12000 and 10000 metal atoms respectively. The main aim of the work with the grain boundaries is to investigate and analyze how bicrystal systems with different orientations and some various coincident lattices affect the thermo-mechanical properties compared to single crystals. Meanwhile, I have used the same EAM interaction potential for all the structures which is NiAl-H interactions included.

To study the influence of hydrogen (H) in nickel-aluminum compound (NiAl) at atomistic length scales, I employed the molecular dynamics simulation method at various temperatures ranging from 0 ^{o}K to 2100 ^{o}K with the increment of 100 ^{o}K to bulk B2, A1, B1 phases of NiAl, along with the L12 phase of Ni$_3$Al (L12 NiAl)and NiAl$_3$ (L12 AlNi) ordered and random single crystal structures and bicrystal structures of B2

and A1 phases of NiAl compounds to investigate the influence of hydrogen through single crystals using embedded atom model potentials to represent the metal-metal and metal-hydrogen interactions. Also, I employed density functional theory (DFT) to the calculations to compare the results of the molecular dynamics simulations with those of the obtained simulations from the vasp code compared to the smaller size structures with the addition of bulk Ni and Al structures separately, which are respectively B1, B2, A1, L12, A4 in one unit cell due to the computationally expensive reasons than the molecular dynamics simulations ascertained from LAMMPS. In the following, describing the employed methods and model constructions for the simulations of the literature review are gathered.

1.3   Compilation of literature on thermo-mechanical properties of NiAl alloys

Due to their exceptional thermo-mechanical properties of NiAl alloys are utilized in many applications ranging from electronics to aerospace industry [3]. The L21 Ni_3Al and B2 NiAl structure were investigated more than other types of crystal structures which possesses splendid properties such as superelasticity, high strength and less density. Moreover, thermodynamic properties of NiAl have investigated via first principles and ab initio methods have had a central role on NiAl to determine its structure and properties. In Table 1, the results on NiAl alloys obtained experimentally and computationally using ab initio DFT methods (some in local density approximation (LDA) and some in generalized gradient approximations (GGA)) to compute the elastic properties, the bulk modulus, the B_0' parameter and the lattice parameter [3].

Table 1: The literature review of elastic properties, the bulk modulus and the other parameters of NiAl intermetallic alloys (in GPa).

Ref	Structure	$a_0(^0A)$	C_{11}	C_{12}	C_{44}	B_0	B_0'
[26]	Ni_3Al		316	202	188	240	
	Ni_3Al		270	141	194	184	
	Ni_3Al		357	239	196	278	
	Ni_3Al		358	237	197	278	
[27]	Al					68.06	
	Ni					191.6	
	NiAl B2					153.5	
	Ni_3Al					182.4	
	Al (exp)					72.2	
	Ni(exp)					186	
	NiAl(B2exp)					156	
	Ni_3Al(exp)						
[13]	Ni_3Al(exp)					161.9	
[28]	Ni_3Al	3.57	368	238	211		
	Ni_3Al	3.57	403	219	201		
	Ni_3Al	3.57	394	219	197		
	Ni_3Al	3.49	376	232	211		
[29]	Al		173	99	45	124	
[30]	NiAl B2	2.89	203	140	113		
	NiAl(exp)	2.89	212	143	112	166	
	NiAl(exp)	2.89	233	121	114	159	
[31]	Ni	3.421	329	153	122		
	Al	4.05	107	62	28.3		
[32]	Al	3.995	92	61	58	71	
	NiAl B2	2.895	261	203	80	222	
	Ni_3Al	3.526	281	207	96	232	
	Ni	3.421	329	218	148	255	
	Al(exp)	4.05	107	61	29	76	
	NiAl(B2exp)	2.886	199	137	116	158	
	Ni_3Al(exp)	3.567	230	150	131	177	
	Ni(exp)	3.523	261	151	132	188	
[33]	NiAl B2	2.84				186	4.2
	Ni_3Al	3.49				229	4.4
	NiAl(B2exp)	2.88					
	Ni_3Al(exp)	3.58					

Table 1 Continued

Ref	Structure	$a_0(^0A)$	C_{11}	C_{12}	C_{44}	B_0	B_0'
[3]	NiAl(B2exp)	2.84				265	4.0
	NiAl	2.88				298	4.2
[34]	NiAl(B2exp)	2.887	199	137	116	156	
	NiAl(B2exp)	2.88	211	143	112	158	
	Ni_3Al(exp)	3.566	169	121	89		
	Ni_3Al (exp)		225	149	124	174	
	$NiAl_3$		232.9	80.3	100	164.7	
[35]	NiAl B2	2.918	172.3	146.1	100.3	154.9	
	NiAl(B2exp)	2.88	199	137	116	158	
	NiAl B2	2.83	185	254	150	133	
	NiAl B2	2.859	222	200	140	120	
	NiAl B2	2.895	178.88	261	203	115.45	
	NiAl B2	2.85	156	199.37	168.41	146	
[33]	NiAl B2	2.84	237	155	132		
	NiAl B2	2.89	193	124	114		
	NiAl B2	2.89	211.5	143.2	112.1		
	Ni_3Al	3.58	227	148	120		
	Ni_3Al	3.58	220.1	146	123.6		

The results as seen can be sometimes different from each other. The reason why the results are different is because the methods and experimental tools that are used can be different. Also the simulation programs make the values also different such as VASP and LAMMPS.

There are also molecular dynamics simulations conducted at different temperatures and calculated thermodynamic properties such as thermal expansion coefficients through averages of volumes at different temperatures. The previous works was divided in two parts, one of them is theoretical values and the other is experimental values. The data are tabulated in Table 2.

Table 2: The experimental and theoretical values of the thermal expansion coefficients of NiAl alloys.

Ref	$\alpha 10^{-6}/K$	Theoretic value	Experimental value
[27]	Al	24.88	23.1
	Ni	12.68	13.1
	NiAl B2	14.06	11.9
	Ni_3Al	12.17	12.3
[32]	Al	26.3	23.6
	$NiAl_3$	25	
	NiAl B2	17.4	10.8
	Ni_3Al	15.9	11.8
	Ni	15.7	12.5

The theoretical and experimental values are almost the same for most of them. However they can also be quite different from each other since the different approximations methods can be set which can cause some variations in results.

2. COMPUTATIONAL METHODS

The computational methods in materials science are critical to describe and understand the behavior of the molecular level structures and the response of the material structures to applied loads (such as pressure or anisotropic stresses), temperature, etc. Especially methods such as molecular dynamics which track the positions, momenta, microscopic state variables such as instantaneous energy, pressure, stress, volume, cell parameters, and even higher order microstate variables such as derivatives aforementioned properties as a function of time. Similarly, inherently more accurate, first principles which is density functional theory (DFT) based methods enable to determine the materials' crystal structure, assess whether they are stable or unstable, or compare their stability with respect to each other, possible phase transitions due to pressure and stress or determine their thermo-mechanical, electrical, physical etc., properties of materials. Hence they provide an alternative or complementary way to experimental studies of materials. Though there are significant advances in imaging and characterization methods and instrumentation, computational approaches at the molecular level provide atomistic level information and through suitable definitions and approaches enable us to determine macroscopic level properties of the materials. The macro level properties of materials and micro level properties of materials are directly related to the one another which means macroscopic properties are a straight outcome of microscopic interactions of materials with the definitions of atomic expressions. These atomic level interactions are in very short time for example, they mostly perform in picoseconds and femtoseconds in computational methods which is very difficult to investigate them with experimental devices because even very tiny alterations can affect the whole result in

experiments which is not desired, the computational methods are inevitably vital to the materials science with the help of theoretical methods and they almost totally complete each other for studying materials. Due to the easiness of computational methods, they have many pros and little cons. For example, they can be done less expensively, don't need big laboratories with many people, occur in very short time but sometimes result can be different from experimental values and having a high error possibility. In atomistic level, quantum mechanics predominates the newton mechanics and cannot be ignored. For quantum level calculations, VASP (Vienna ab-initio simulation package) which is a code to perform ab initio methods in molecular dynamic and for Newtonian level calculations, LAMMPS (large-scale atomic or molecular simulation package) that is also a code to perform classical mechanics, are used in my studies.

2.1 Density functional theory

Density functional theory (DFT) is a quantum level description of the material system of interest [36]. Nevertheless, it is not only a regular approach to derive and solve the time independent Schrodinger equation but totally distinct based on an genuine way simplifying many body quantum problems and still quite a costly way to solve any large scale problems [37, 38]. For instance, they are model systems involving defects [39]. Therefore, the interest on DFT calculations has tremendously increased in materials science and related areas for a few decades and succeeded itself in numbering published papers however the roots of the DFT methods have a longer history than that of time interested in along with incorporating with molecular dynamics methodology come as

13

reasonable results of how reactive crystal systems are related to each other, and so are the bigger systems such as polymers [40, 41].

Time independent Schrodinger equation [37];

$$\left[-\frac{\hbar^2}{2m}\frac{\partial^2\Psi(x)}{\partial^2 x} + V(x) = E\Psi(x)\right] \tag{1}$$

The solution of Schrodinger equation, which is not relativistic, of Born-Oppenheimer approximation is [37, 42];

$$H\Psi(r_1, r_2 \dots r_N) = E\Psi(r_1, r_2 \dots r_N) \tag{2}$$

H is Hamiltonian which is composed of basically three parts. The first part is the kinetic energy term, the second part is the potential energy term and the last part is the interaction energy term between electrons shown below briefly [37].

$$H = -\frac{1}{2}\sum_i^N \nabla_i^2 + V_{ext} + \sum_{i<j}^N \frac{1}{|r_i - r_j|} \tag{3}$$

The potential energy term which is external is actually the result of interactions between electrons and nuclei. The r_i term is the position of the ith electron in the atom with the charge of Z_α from R_α [37].

$$V_{ext} = -\sum_{\alpha}^{N_{at}} \frac{Z_\alpha}{|r_i - R_\alpha|} \tag{4}$$

The whole energy of a certain system by Ψ as the expectation value of H is specified.

$$E[\Psi] = \int \Psi^* H \Psi \, dr \equiv \langle \Psi|H|\Psi \rangle \tag{5}$$

The E_0 is the minimum energy at ground state. The variational theory condition is;

$$E[\Psi] \geq E_0 \tag{6}$$

The Hartree Fock (HF) system consists of the functions ϕ_i that are antisymmetric yields of every initial position of electrons at the ith coordinate [37].

$$\Psi_{HF} = \frac{1}{\sqrt{N}} \det[\phi_1 \phi_2 \phi_3 \dots \phi_N] \tag{7}$$

This equation turns out be the following form of the energy of the system called Hartree Fock energy which is really important to include the quantum behavior for initial positions [37].

$$E_{HF} = \oint \phi_r^*(r) \left(-\frac{1}{2} \sum_i^N \nabla_i^2 + V_{ext} \right) \phi_i r \, dr$$

$$+ \frac{1}{2} \sum_{ij}^N \oint \frac{\phi_i^*(r_1)\phi_i(r_i)\phi_i^*(r_2)\phi_j(r_2)}{|r_i - r_j|} dr_1 \, dr_2 \qquad (8)$$

$$- \frac{1}{2} \sum_{ij}^N \oint \frac{\phi_i^*(r_1)\phi_i(r_i)\phi_i(r_2)\phi_j^*(r_2)}{|r_i - r_j|} dr_1 \, dr_2$$

The second part is HF energy formula that is Coulomb's interaction energy and the last part of that is exchange energy of the system. After applying the variational theory it comes as HF equations below. The (r_i) is the probability of density of electrons at certain positions [37].

$$\left[-\frac{1}{2}\nabla^2 + V_{ext}(r) + \int \frac{\rho(r')}{|r - r'|} \right] \phi_i(r) + \int V_X(r, r')\phi_i(r') \, dr' = \varepsilon_i \phi_i(r) \qquad (9)$$

After this point, Ψ the minimum energy of the system can be ascertained with the variations of computational cost. This method can be and is used in many different problems such as electronic structure, binding energy calculations in solid state physics. DFT accomplishes what Hartree Fock (HF) method, which are traditionally and heavily used molecular level computations, cannot do by using the electronic density instead of electronic wave functions [43, 44]. Although the wave function is related to 3N variables in N electron group the electron density has just three variables that usher to a much

simpler way of reaching out to desired quantities with indirectly connected electron correlation. Quite a few methods and correlations have been established from these equations such as MP2, MP4, CCSD etc. but not all of them are useful to employ due to the computational costs [37].

According to Hohenberg and Kohn, DFT is based on two vital theorems. The first one is that the electronic wave function and all other properties in the electronic system are found out through the electron density. The second theorem explains that the electron energy distribution can be functionally expressed, which is the minimum energy of the ground state density [37, 43]. Kohn-Sham equations possess the same procedure like HF from variational theory [37, 39].

$$\int \rho_t(r) \, dr = N \tag{10}$$

As a result of Kohn–Sham system, energy formalism becomes;

$$E[\rho] = T[\rho] + V_{ext}[\rho] + V_{ee}[\rho] \tag{11}$$

The V_{ee} and V_{ext} symbols are respectively external potential energy and interaction energy of electrons [37].

$$V_{xc}(r) = \frac{\delta E_{xc}[\rho]}{\delta \rho} \tag{12}$$

17

The exchange correlation energy of system is related to the density function now. The theory is based on how to use approximations to obtain the exchange correlation energy.

2.2 Molecular dynamics

Molecular dynamics for classical mechanics is a widely used computer simulation method which simulates the behavior of materials through the interactions between particles (atoms to be more specific) to study larger scale problem directly on systems containing defects, impurities, heterogeneities, such as surfaces, interfaces, dislocations, grain boundaries, pores, etc. Its core is to solve the equations of motion for a collection of atoms within the model system through evaluating the forces on them arising from interatomic interactions [45] such as local density approximation [23]. A materials property depends on its micro level size behaviors and relations to how they atomistically interact with one another. These phenomena happen at extremely short time intervals that can only be defined in picosecond or femtosecond breaks. A widespread belief is that a materials' property is correctly determined by only experiments which is very difficult to do them in this much short time intervals where molecular dynamics simulations come as inevitable methods to perform. By using the classical equations of motion one would obtain the configurations and associated momenta of collection of the atoms in time. The microscopic statistical mechanical descriptions of physical properties are averaged over time (or in commonly used term over the trajectory) to obtain physical properties of the system under consideration. This method is extremely convenient for condensed phase problems have been used since its inception in late 1950s. Suppose that many of

18

particles in a box are interacting by themselves with relative motion with the reduced

mass μ.

$$f_{ij} = \mu a_{ij} \qquad (13)$$

$$r_{ij} = r_j - r_i \qquad (14)$$

The r_{ij} is the distance vector between ith particle and jth particle and f_{ij} is the force on

ith particle due to jth particle. The important part is how to express the particles that are

interacting with one another. Shortly, the input properties, boundary conditions and

newton equations which are requirements are respectively determined the evolution of

the system.

The interactions of atoms in simulations have potential energies addressed by classical

potentials (most commonly used empirical pair potential is the Lennard Jones

potential Φ [15] :

$$\Phi(r_{ij}) = 4\varepsilon\left(\left(\frac{\sigma}{r_{ij}}\right)^{12} - \left(\frac{\sigma}{r_{ij}}\right)^{6}\right) \qquad (15)$$

The r_{ij} is the distance between jth and ith atoms along with σ is the potential length

parameter equivalent to the effective diameter of the atom.

$$r_{ij} = \overrightarrow{|r_{ij}|} = |\vec{r}_j - \vec{r}_i| \qquad (16)$$

The physical quantities, could be as diverse as possible, some of which are internal energy, pressure, stress, polarization, elastic constants, diffusion, vibrational spectra, and many others can be expressed through microscopic statistical formulas in terms of coordinates and momenta, using appropriate statistical averaging one can determine the associated macroscopic property, and can be directly compared to experiments. Hence, the simulations generate bulk properties on the basis of molecular level interactions. To obtain reliable results, the boundary conditions pertaining to experimental conditions must be specified and specific form of the molecular dynamics form has to be conducted. To list most common ones of these external conditions; pressure/stress, and temperature. Through solving classical equations of motion, molecular dynamics generates a temporally evolving positions and velocities as the key data, which is used in analyzing properties of interest. To establish the connection between microstates of the systems and macroscopic properties one uses averaging. Some of them are NVE that has an isochoric system means microcanonical ensemble and no change in volume, energy and moles. The next one is NVT one of mostly used having isothermal meaning canonical ensemble, no change in temperature volume or energy known as constant temperate simulations.

In classical molecular dynamics the reliability of simulation results is determined by how well interactions between atoms are described, in other words, how reasonable the chosen functional form for the interactions is and how accurately the associated

20

parameters are determined for the functional form [15]. For metals, the embedded atom

model (EAM) many body interaction potentials have been widely accepted reliable form

of interaction force fields.

2.2.1 Verlet algorithm

The time evolution of positions, velocities, and forces is central to MD calculations.

Hence to evolve the atomistic configurations in simulation, the equation of motion of the

many body system must be solved numerically in discrete time steps accurately. There

are many algorithms in common molecular dynamics. Among these, the most widely

used one is the Verlet algorithm that is hence used for solving the Newtown's equation

of motion. The plain logic of Verlet algorithm is to expand the position and/or velocity

as a Taylor series expansion series in Δt forward and backward as shown simply below;

$$r(t + \Delta t) = r(t) + v(t)\Delta t + \frac{1}{2}a(t)\Delta t^2 + \frac{1}{6}b(t)\Delta t^3 + O\Delta t^4 \qquad (17)$$

$$r(t - \Delta t) = r - v(t)\Delta t + \frac{1}{2}a(t)\Delta t^2 - \frac{1}{6}b(t)\Delta t^3 + O\Delta t^4 \qquad (18)$$

Adding equation (17) and (18) resulting the equation (19);

$$r(t + \Delta t) = 2r(t) - r(t - \Delta t) + a(t)\Delta t^2 + O\Delta t^4 \qquad (19)$$

$$r(t + \Delta t) = r(t) + v(t)\Delta t + \frac{1}{2}a(t)\Delta t^2 \qquad (20)$$

$$a(t) = \frac{1}{m}\nabla V(r(t)) \qquad (21)$$

2.2.2 Embedded atom model potentials

Embedded atom model comes out as an approximation technique to the energy of metal atoms which are interacting in a many body systems [46]. EAM has two core advantages to pair-potential, which eliminate the Cauchy equality arising in 2-body potentials and reproducing proper cohesive energy and vacancy formation values one might have difficulty in reproducing by many 2-body interaction potentials. As an earlier attempt to many body interactions put forth through a mathematical formula by Finnis and Sinclair using the second-moment approximation in the tight binding theory. The fundamental formulas interaction energy for EAM are [46] given as in the following;

$$E_{tot} = \sum_i E_i \tag{22}$$

$$E_i = F_i(\rho_i) + \frac{1}{2}\sum_i \emptyset_{ij} E_i\left(r_{ij}\right) \tag{23}$$

$$E_i = F_i(\rho_i) + \frac{1}{2}\sum_i \emptyset_{ij} E_i\left(r_{ij}\right) \tag{24}$$

The E_{tot} is total internal energy of the whole atoms in the area , E_i is internal energy of atom i, ρ_i is total electron density of atom I $\emptyset_{ij}$ is the potential between I and j $F_i(\rho_i)$ is the energy of embed atom I r_{ij} is distance $f_i\left(r_{ij}\right)$ is the electron density at r_{ij} [46].
In this study, I have performed molecular dynamics using LAMMPS code with EAM potential developed for the NiAl alloys and H in NiAl alloys.

3. THERMO-MECHANICAL PROPERTIES OF NiAl ALLOYS

3.1 Mechanical properties from DFT

To investigate the energetics, structure and mechanical properties of the NiAl alloys in the L10, B2, A4, B1 and L12 structures and their concentrations. I have used the VASP code for DFT calculations.

First off, I constructed POSCAR by finding the atoms' positions in the crystals and the lattice parameters which I calculated from the following composition rules to start constructing the POSCAR file.

The a is the lattice constant, V is the volume, ρ is the density, N_{av} is the Avogadro number;

$$\rho = \frac{(A_{Ni} + A_{Al})}{N_{av} * V} \tag{25}$$

$$V = a^3 \tag{26}$$

$$a = \sqrt[3]{\frac{(A_{Ni} + A_{Al})}{N_{av} * \rho}} \tag{27}$$

After determining starting lattice parameters where there is no data as described above, I chose KPOINTS as a 10x10x10 mesh-cell which I would optimize later and change the mesh-cell value. Lastly but not the least, I have constructed INCAR file with

a variable encut (energy cut off) value and then, respectively I optimized encut, and

KPOINTS to have an accuracy level within a few MeV per atom. I have developed

energy vs. volume, pressure vs. volume data through which I fit data to Birch

Murnaghan Equation of State (EOS) equations given below and determined the zero

stress-pressure volume (lattice parameter), bulk modulus and pressure derivative of bulk

modulus from the fit.

The third order Birch Murnaghan equations for pressure and energy are given below:

$$P(V) = \frac{3B_0}{2} \left[\left(\frac{V_0}{V}\right)^{\frac{7}{3}} - \left(\frac{V_0}{V}\right)^{\frac{5}{3}} \right] \left\{ 1 + \frac{3}{4}(B_0' - 4) \left[\left(\frac{V_0}{V}\right)^{\frac{2}{3}} - 1 \right] \right\} \qquad (28)$$

$$E(V) = E_0 + \frac{9B_0V_0}{16} \left\{ \left[\left(\frac{V_0}{V}\right)^{\frac{2}{3}} - 1 \right]^3 B_0' + \left[\left(\frac{V_0}{V}\right)^{\frac{2}{3}} - 1 \right]^2 \left[6 - 4\left(\frac{V_0}{V}\right)^{\frac{2}{3}} \right] \right\} \qquad (29)$$

P is the pressure, V_0 is the reference volume, V is the volume variable, B_0 is the bulk

modulus, and B_0' is the derivative of the bulk modulus with respect to pressure. The

internal energy is E.

Based on the symmetry of the system the calculated bulk modulus can be related to

elastic constant components, for instance in cubic systems. In order to obtain tetragonal

shear and pure shear elastic constants, I have imposed tetragonal shear strain and pure

shear strain to the system, positive and negative values in discrete steps. From the strain

energy-strain (equivalently stress-strain) relationships, I have obtained the tetragonal

shear constant (C_t) and pure shear constant (C_{44}) which I utilized to find components of

elastic constants: C_{11}, C_{12}, C_{44}. By using the stability conditions determined the mechanical stability of each crystalline form I have modeled. I also compared these values with previously obtained values that are experimental and computational ones.

Mechanical properties are challenging to evaluate its stability due to the complexity of its polycrystalline structures. Ab initio calculations have a good approach to determine the mechanical properties accurately. To compute elastic constants, it is in the epicenter of mechanical stability due to the relations of most other properties having ties with elastic constants. Elastic constants can be computed by two ways accurately giving reasonable results one of which is related to the energy and its function parameters of pressure or choosing volume instead of the other, as regards strains applied [47].

$$E(V, \varepsilon) = E(V_0) + V \sum_{i=1}^{6} \sigma_i \, \varepsilon_i + \frac{V}{2} \sum_{i,j=1}^{6} C_{ij} \varepsilon_i \varepsilon_j + \cdots \tag{30}$$

The other way to compute elastic constants is the stress and strain relation which one can expand it to second, third or fourth order with applying stress in return resulting in strains changes. Every time, there is a deformation stress which is computed as matrix formalism. Hooke's law is very common to obtain stress-strain tensors.

$$\sigma_i = \sum_{j=1}^{6} C_{ij} \, \varepsilon_j \tag{31}$$

To solve this linear equation we need to apply various strains to the system to construct a set of linear equations for each unknown component of elastic constants. For a general system with no symmetry, the total number of nonzero elastic constants is 36, but due to symmetries of elastic constant tensor, the number of independent elastic constants is reduced to 21. For a cubic system due to high symmetry, the number of elastic constants is further reduced down to three.

In general, the elastic constant tensor is can be represented as a 6x6 matrix with Voigt notation.

$$C_{ij} = \begin{pmatrix} C_{11} & C_{12} & C_{13} & C_{14} & C_{15} & C_{16} \\ C_{21} & C_{22} & C_{23} & C_{24} & C_{25} & C_{26} \\ C_{31} & C_{32} & C_{33} & C_{34} & C_{35} & C_{36} \\ C_{41} & C_{42} & C_{43} & C_{44} & C_{45} & C_{46} \\ C_{51} & C_{52} & C_{53} & C_{54} & C_{55} & C_{56} \\ C_{61} & C_{62} & C_{63} & C_{64} & C_{65} & C_{66} \end{pmatrix} \qquad (32)$$

Using the symmetries of the cubic systems.

$C_{11} = C_{22} = C_{33}, C_{12} = C_{21} = C_{31} = C_{32} = C_{23} = C_{13}$ and $C_{44} = C_{55} = C_{66}$

$0 = C_{14} = C_{15} = C_{16} = C_{26} = C_{25} = C_{24} = C_{34} = C_{35} = C_{36} = C_{46} = C_{45} = C_{56} = C_{41} = C_{42} = $

$C_{43} = C_{51} = C_{52} = C_{53} = C_{54} = C_{61} = C_{62} = C_{63} = C_{64} = C_{65}$

Now it turns out to be the following equation;

$$C_{ij} = \begin{pmatrix} C_{11} & C_{12} & C_{12} & 0 & 0 & 0 \\ C_{12} & C_{11} & C_{12} & 0 & 0 & 0 \\ C_{12} & C_{12} & C_{11} & 0 & 0 & 0 \\ 0 & 0 & 0 & C_{44} & 0 & 0 \\ 0 & 0 & 0 & 0 & C_{44} & 0 \\ 0 & 0 & 0 & 0 & 0 & C_{44} \end{pmatrix} \tag{33}$$

To determine C_{11}, C_{12}, C_{44} one needs to apply only three forms of strains to a cubic system. An isotropic dilatational strain, in order to obtain the bulk modulus;

$$\delta_t = \begin{pmatrix} \delta & 0 & 0 \\ 0 & \delta & 0 \\ 0 & 0 & \delta \end{pmatrix} \tag{34}$$

 To obtain the tetragonal shear elastic constant, one can apply the following tetragonal shear strain tensor;

$$\delta_t = \begin{pmatrix} \delta & 0 & 0 \\ 0 & -\delta & 0 \\ 0 & 0 & \Delta \end{pmatrix} \tag{35}$$

The Δ parameter is determined from the volume conservation under applied strain;

$$\Delta = \frac{\delta^2}{1 - \delta^2} \tag{36}$$

To ascertain the C_{44} or pure shear elastic constant one could apply the following pure shear strain tensor to the model system.

$$\delta_{44} = \begin{pmatrix} 0 & \delta & 0 \\ \delta & 0 & 0 \\ 0 & 0 & \Delta \end{pmatrix} \tag{37}$$

The form of the Δ is specifically chosen to preserve the volume is the same as in. After converting strain tensor to Voigt notation and computing the strain energy in terms of strain, leaving terms up to the second order we have:

For the tetragonal shear strain energy with only $O(\delta^4)$ is the error;

$$\Delta E = 6C_t V_0(\delta^2) + O(\delta^4) \tag{38}$$

For the pure shear strain energy the error is the same;

$$\Delta E = 2C_{44}V_0(\delta^2) + O(\delta^4) \tag{39}$$

The relation between the tetragonal shear constant, C_{11} and C_{12} is;

$$C_t = \frac{C_{11} - C_{12}}{2} \tag{40}$$

The relation between bulk modulus, C_{11} and C_{12} is;

$$B_0 = \frac{C_{11} + 2C_{12}}{3} \tag{41}$$

Using these equations for C_{11} and C_{12} are readily calculated and results are expressed in units of GPa, after conversion units from eV/A3 [48].

$$\frac{eV}{A^3} = 160.21766208 \text{ GPa} \tag{42}$$

After the conversion of the elastic constants, bulk modulus, B_0' and lattice parameters obtained from the DFT calculations, are tabulated in Table 3.

Table 3: Elastic constants, lattice parameters, bulk moduli and the other parameters of the NiAl alloys and Ni, Al metals from DFT calculations.

Structure	$a_0(^oA)$	$C_{11}(GPa)$	$C_{12}(GPa)$	$C_{44}(GPa)$	$B_0(GPa)$	B_0'
Al	3.98	97.34986	83.06105	51.19369	87.82399	3.86
NiAl$_3$	3.78	154.7664	114.5115	34.58577	127.9298	3.75
NiAl(L10)	3.59	197.7198	175.8405	182.4868	183.1336	3.72
Ni$_3$Al(L12)	3.48	252.892	219.057	152.7992	230.3353	3.70
Ni	3.42	281.6308	245.8507	148.6413	257.7774	3.81
NiAl(B1)	4.75	183.887	109.3516	-4.26319	134.1967	3.84
NiAl(A4)	5.22	77.29312	83.33932	43.56265	81.32392	3.87
NiAl(B2)	2.83	215.7415	172.4413	121.0056	186.8747	3.71

The minimum energy is computed for one aluminum and nickel atom and for pure aluminum and nickel, it is computed per two atoms. The lowest energy is theoretically the most stable structure which proves that B2 crystal structure is one of the most stable structure and B1 structure is the least stable structure which also agrees with the

elasticity condition that B1 does not satisfy and C44 value has a negative value that does

not satisfy either.

Table 4: The energy differences for the stability of NiAl structures obtained from the
subtraction of pure Ni and pure Al energies.

Structure	Energy (eV)	Delta Energy
Al	-8.37095	--
NiAl(B2)	-12.1990	-1.4756
NiAl(A4)	-9.69585	1.0276
NiAl(L10)	-11.8728	-1.1494
NiAl(B1)	-10.8647	-0.1413
$NiAl_3$(L12)	-10.0277	-0.481
Ni_3Al	-12.9034	-1.0033
Ni	-13.0768	--

Upon obtaining the energy differences of structures which gave the delta energy, these

values are shown in Figure 2 with respect to the total energies of the structures.
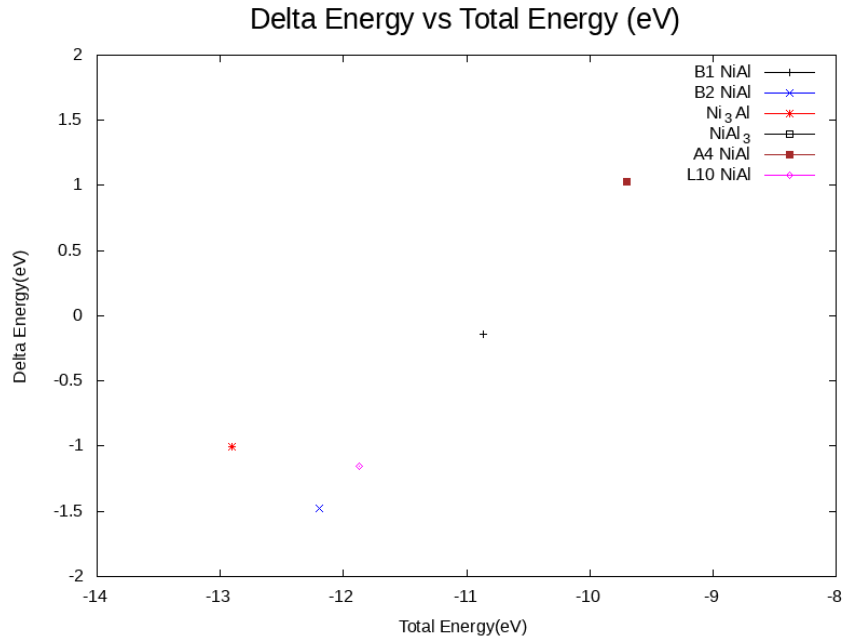
Figure 2: The dots show that the delta energy and total energy of the NiAl structures for stability.

After obtaining the results, I have to check the mechanical stability using the

following conditions for cubic systems which are;

$$C_{11} - C_{12} > 0 \qquad (43)$$

$$C_{44} > 0 \qquad (44)$$

As it is seen, the NiAl B1 structure does not satisfy equation (44) and NiAl A4 also does

not satisfy equation (43). Therefore, these two crystalline structures are not mechanically

stable under the shear stress and tetragonal stress loads respectively.

3.2 Mechanical properties from MD

3.2.1 NiAl structures for mechanical properties from MD

To calculate thermodynamic and mechanical properties of various crystalline forms of NiAl, we have conducted molecular dynamics simulations. The model systems are built from unit cells of each crystalline structures by creating super cells. The model size for B1 is 8000 atoms total obtained from a 10x10x10 super cell. The system is gradually heated from 0 ^{o}K to 2100 ^{o}K creating models to use at each 100 ^{o}K steps in order to obtain the thermal properties as a function of temperature (Energy or Enthalpy vs. T), (Volume vs. Temperature); (Volume vs. Pressure); each of which used to determine the specific heat capacity, and thermal expansion. At certain temperatures (100 ^{o}K, 300 ^{o}K, 500 ^{o}K, 700 ^{o}K) to determine pressure vs. volume behavior, I have applied pressure-stress on the system ranging from 0.1 GPa to 5 GPa in all directions isotropically. Note that, I have used the well equilibrated initial structures from the end of the equilibrium runs we computed the energy vs. temperature, and volume vs. temperature behavior earlier. I have determined the bulk modulus from volume pressure curves at each temperature. To develop data for anisotropic mechanical response or elastic constants at elevated temperatures I have imposed the compressive stress in x direction and I obtained compression modulus from the variation of Lx (length of model in x-direction) vs. pressure behavior. I also determined the tensile modulus on the same system by imposing tensile stress.

I have employed the same set of calculations to B2, A1 and L12 structures as well.

The B2 model size is 8192 atoms constructed from the unit cell as a 16x16x16 super cell

of B2. The A2 and L12 structures totally have 4 atoms that one eighth at every corner

and one half on every face. I have built a 13x13x13 super cell of A1 and L12 which have

total 8788 atoms. I have also constructed L12 structures in ordered and random alloys

forms.

3.2.2 Bulk modulus of NiAl alloys from MD simulations

The bulk modulus is computed from volume vs. pressure behavior obtained from

molecular dynamics simulations at various temperatures.

$$B_0 = -V\left(\frac{\partial P}{\partial V}\right) \tag{45}$$

The volumetric change in the NiAl structures are investigated through the bulk modulus

change from the hydrostatic pressure tests which performed from 0 GPa to 5 GPa and

data collected for every time step and noted through the simulations for 200000

timesteps.

For hydrostatic pressure test, three steps applied first the increment of pressure for

50000 timesteps and it relaxed for 50000 timesteps after that, data is ready to be

collected. After these procedures, the runs performed and obtained trajectory files which

would give the raw data. Therefore, I averaged the raw data to obtain the bulk modulus

values.

Table 5: The bulk modulus of the NiAl structures at 100 K, 300 K, 500 K and 700 K.

Structure	100 °K	300 °K	500 °K	700 °K
L10Σ 5 (210)	164.6744	155.9435	148.5508	143.4875
L10Σ 5 (310)	164.7935	155.6965	148.6426	143.4083
L10Σ 3 (210)	134.807	124.169	122.6387	110.795
B2Σ 5 (210)	177.963	170.2375	161.2612	149.6148
B2Σ 5 (310)	177.963	170.2375	161.2612	149.6148
B2Σ 3 (210)	181.2472	165.0367	146.5902	139.1917
NiAl B2	182.4805	175.3902	167.1696	156.8212
NiAl B1	135.0959	132.8173	117.7097	91.73186
Ni_3Al	170.1065	159.0954	147.1424	136.628
$NiAl_3$	147.5059	148.3096	143.8452	133.1246
$NiAl_3$ R L12	118.9861	110.4559	96.02685	71.50799
NiAl R L10	119.9422	121.2007	122.9423	122.693
Ni_3Al R L12	153.1922	135.7242	121.5307	112.7661

I have employed the NPT ensemble by imposing isotropic pressure and averaged the variation of volume at each temperature, 100 °K, 300 °K, 500 °K and 700 °K, for the applied pressure values starting from 0.1 GPa to 5 GPa. For the bicrystal systems, I have used the same pressures in NPT ensemble simulations and at the same temperatures 100 °K, 300 °K, 500 °K and 700 °K which I obtained the initial structures from the heating-up simulations to be used in the hydrostatic applied pressure runs for considering the fluctuations and other effects, which can have a big role in determining the bulk modulus, which were deeply investigated in the heating-up runs for 200000 timesteps to be equilibrated after the increment and relaxation of the same temperature.
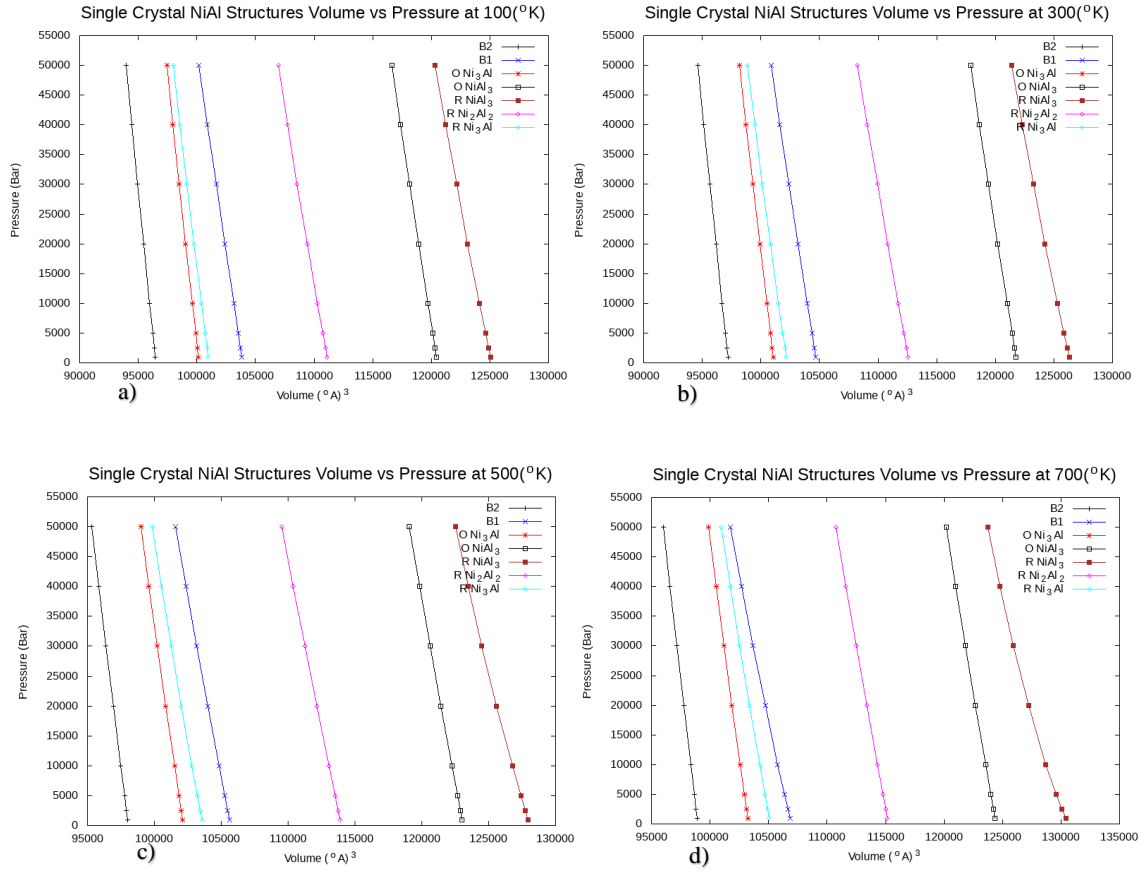
Figure 3: The variation of volume under the hydrostatic pressure from 0 GPa to 5 GPa a) at 100 K, b) at 300 K, c) at 500 K, d) at 700 K.

The B2 NiAl structure has the highest bulk modulus value, on the other side the B1 NiAl structure has the lowest bulk modulus value at $100\,^{\circ}K$. Once the temperature started to increase the bulk modulus values decreased at different amounts. The $NiAl_3$ has been affected the least among single crystals however from $100\,^{\circ}K$ to $700\,^{\circ}K$. However, the structures also were affected at different proportions from $500\,^{\circ}K$ to $700\,^{\circ}K$ from $100\,^{\circ}K$ to $300\,^{\circ}K$ or $300\,^{\circ}K$ to $500\,^{\circ}K$.
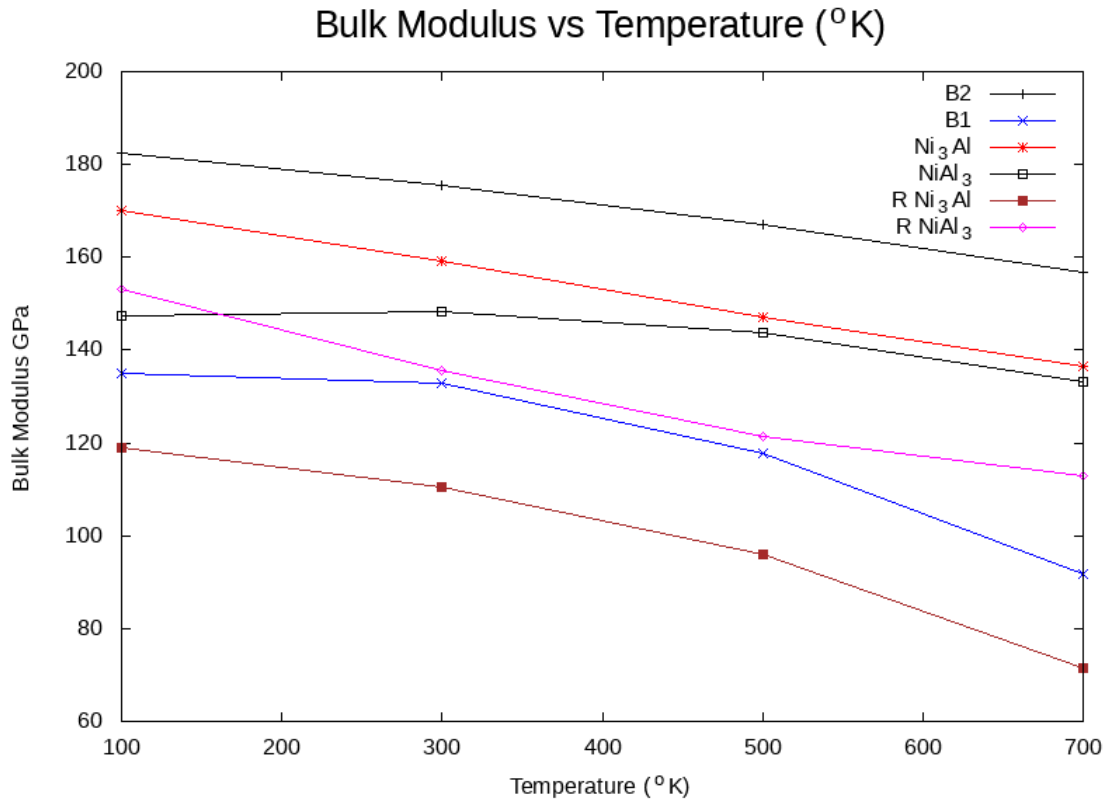
Figure 4: The variation of bulk modulus as a function of temperature for single crystal models.

The transition temperature from 300 ^{o}K to 500 ^{o}K for bulk modulus has affected most B1 and R Ni$_3$Al structures and from 100 ^{o}K to 300 ^{o}K has not changed the bulk modulus significantly. However, once it has come up to 700 ^{o}K it decreased mostly almost all the structures. The NiAl$_3$ structure showed very little change unlike other structures at 300 ^{o}K but at 500 ^{o}K and 700 ^{o}K it changed significantly as the other structures.
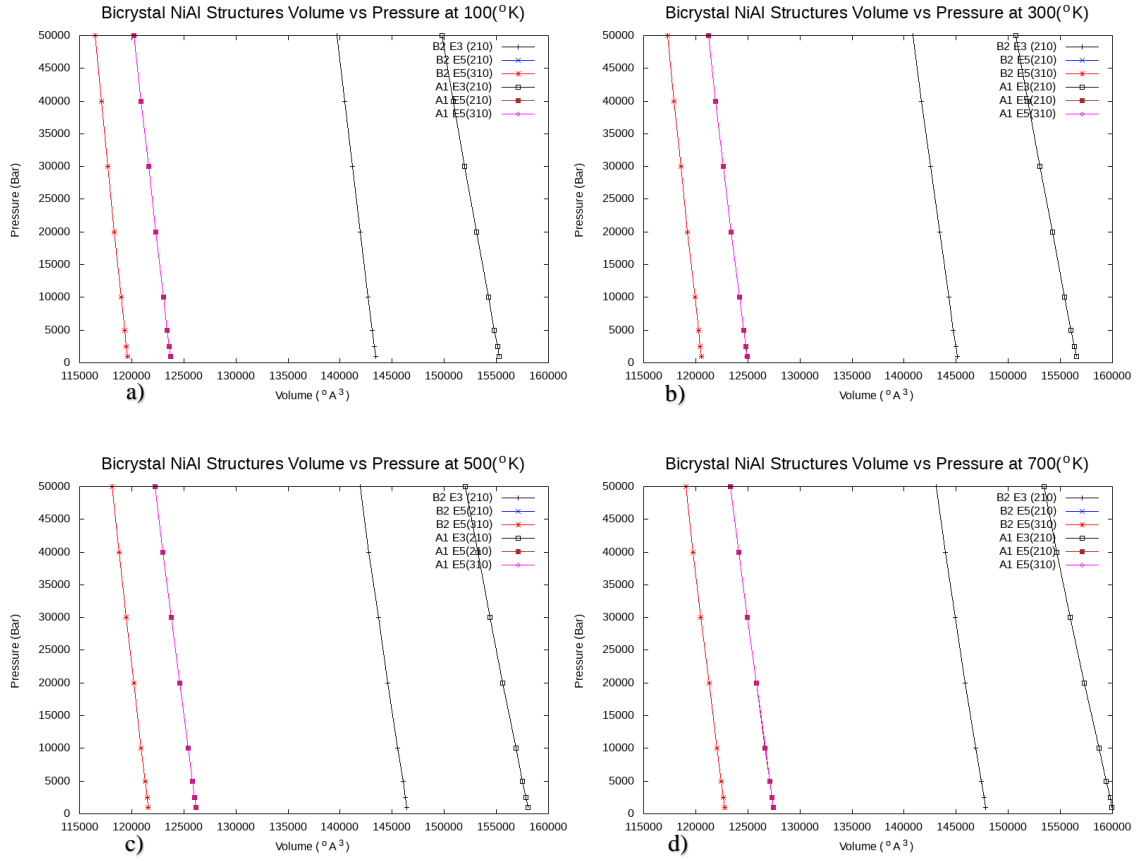
Figure 5: The bicrystal structures are investigated for bulk modulus under the hydrostatic pressure from 0 GPa to 5 GPa a) at 100 K, b) at 300 K, c) at 500 K, d) at 700 K.

The grain boundary structures for bicrystal systems were also investigated and the different planes for the same structures had the same bulk modulus. The bulk modulus of the B2 Σ 3 structure is the highest, on the other side the bulk modulus of the L10 Σ 3 is the lowest at 100 °K. However, the structures showed an interesting thing which was the highest value of the bulk modulus at 100 °K decreased most at 700 °K and the lowest bulk modulus at 100 °K decreased least at 700 °K.

Bulk Modulus vs Temperature (^{o}K)
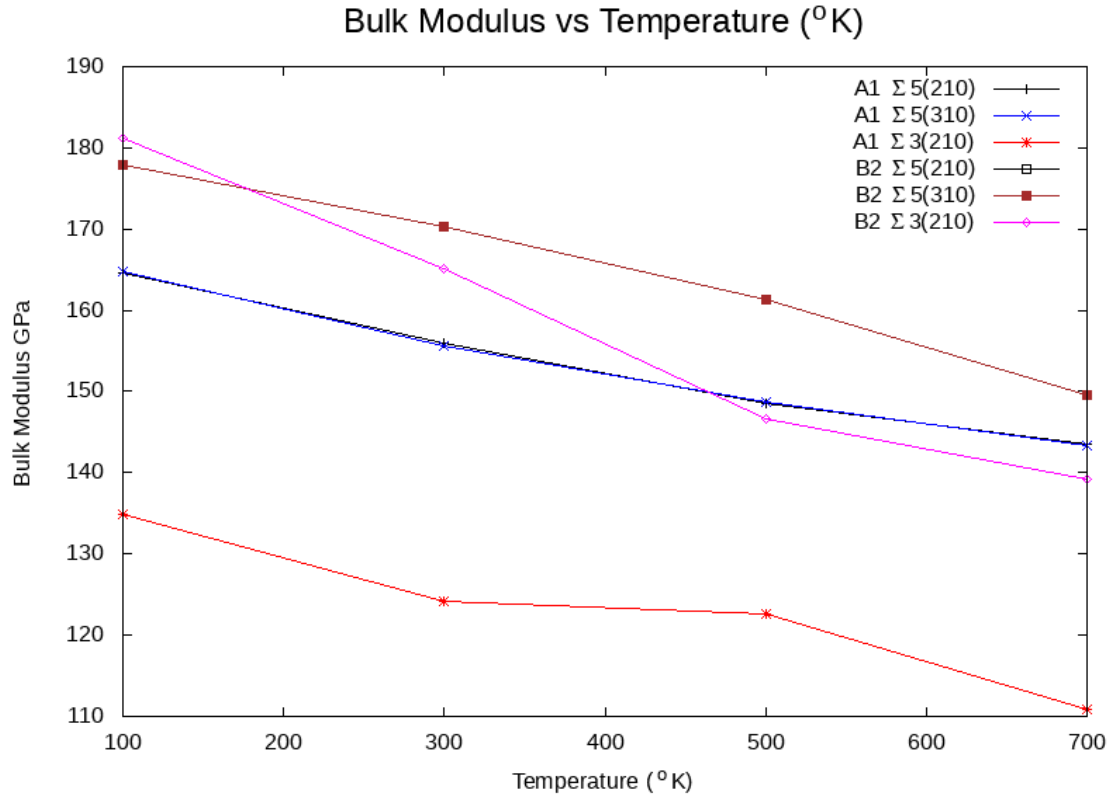
Figure 6: The bulk modulus of the same structure with different planes had the same bulk modulus and decreased the same amount at the different temperatures.

3.2.3 Uniaxial stress tests in NiAl alloys and modulus

The modulus is the ratio of stress to strain. I have imposed the compressive stress test in x direction ranging from 0.1 GPa to 5 GPa in NPT ensemble at 100 ^{o}K, 300 ^{o}K, 500 ^{o}K, 700 ^{o}K temperatures. The stress free structures at each temperature are obtained from the atmospheric pressure from heating up simulations at the corresponding temperatures. The tensile tests are similar to compression tests. This systems were pulled along x direction by applying stresses ranging from 0.1 GPa to 5 GPa. The original stress free states chosen the same way as described above. The simulations are conducted at 100

ºK, 300 ºK, 500 ºK and 700 ºK that are from the end of the heating up relaxation temperatures of the simulations. The modulus is computed using;

$$\text{Young Modulus} = \frac{\sigma}{\epsilon} = \pm \frac{P_{xx}}{(L_x - L_{x0})/L_{x0}} \qquad (46)$$

L_{x0} is the initial value of x-dimension of the model system, and L_x is the length after deformation due to applied stress, P_{xx} is the applied stress along x direction.

Table 6: The compression and tension tests resulting in young modulus with respect to temperature for bicrystal and single crystal structures.

Structure	100 ºK	300 ºK	500 ºK	700 ºK
L10Σ 5 (210)	144	134	120	100
L10Σ 5 (310)	144	134	120	100
L10Σ 3 (210)	58	43	37	17
B2Σ 5 (210)	57	53	51	50
B2Σ 5 (310)	57	53	51	50
B2Σ 3 (210)	180	171	154	138
NiAl B2	116	114	110	103
NiAl B1	56	43	34	17
Ni_3Al	149	131	109	103
$NiAl_3$	90	88.3	82	68
$NiAl_3$ R L12	71	63	57	41.3
Ni_3Al R L12	107	96	83	67
NiAl R L10	79	77	75	73

The young modulus values are found from the slope of the compression-tension pressure and the amount of the increase in the x direction. The young modulus decreased as the temperature increased as bulk modulus.
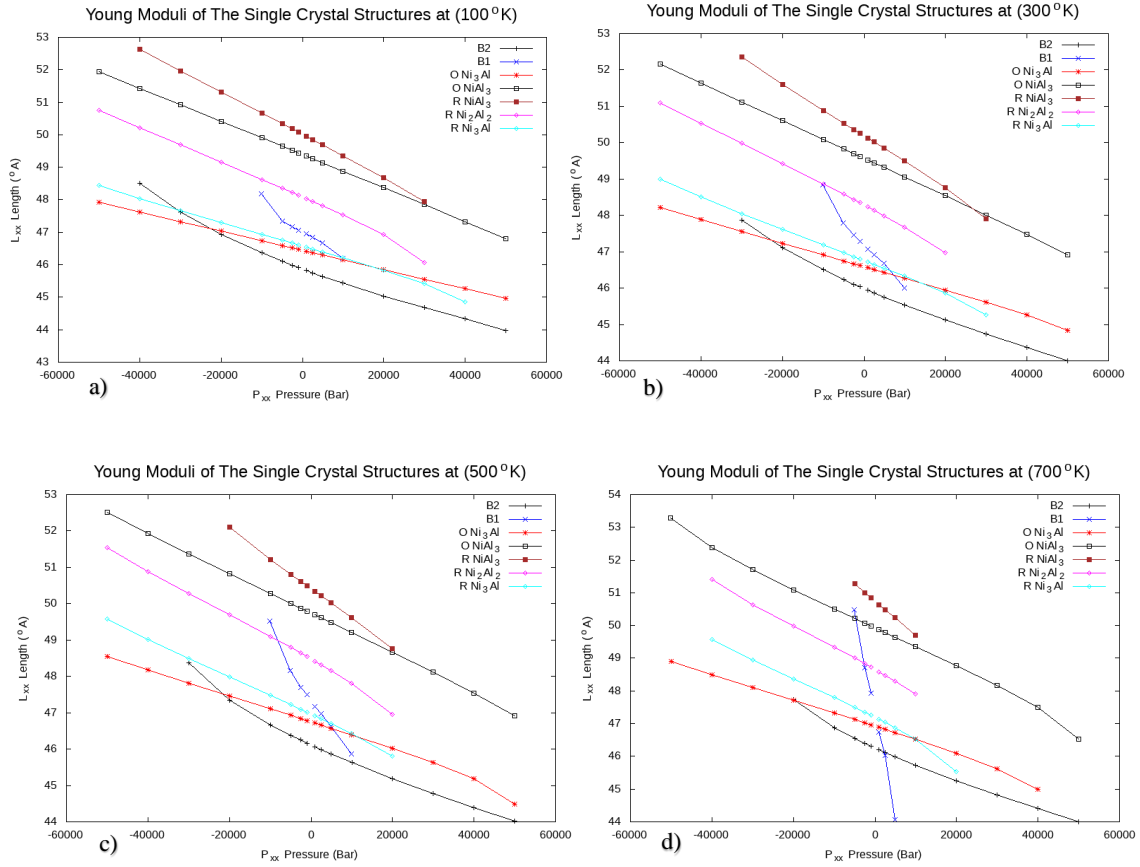
Figure 7: The uniaxial compression-tension tests in single crystal systems at a) 100 K, b) 300 K, c) 500 K and d) 700 K.

The compression-tension tests applied in the x direction with the opposite directions and the slope decreased as the temperature increased which showed the young modulus and the yield strength are not considered these values are in the elastic limits. The B1 NiAl structure decreased a lot and almost lost all of its modulus. The structures that were more stable were affected less comparatively. The linearity of the young modulus changes as well when temperature increases and this property is more visible at 700 $^{\circ}$K than the others.
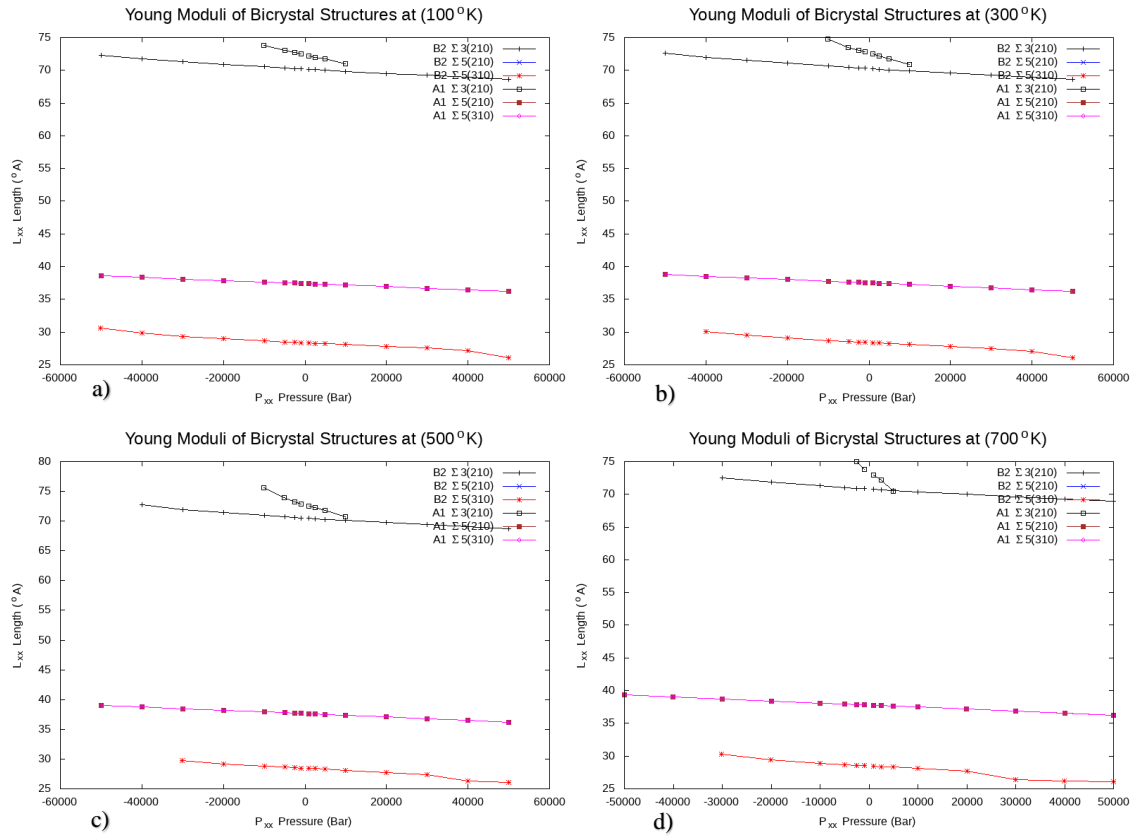
Figure 8: The bicrystal structures shows the young modulus change from the compression and tension tests at a) 100 K, b) 300 K, c) 500 K and d) 700 K.

In the bicrystal cases, tensile stress tests are conducted for all the structures. As bulk modulus, temperature had affected young modulus negatively. In bicrystal systems, the young modulus values are more distant in comparison with that of single crystal structures due to the direction of the grain boundary.

41

3.3 Thermal properties from molecular dynamics

3.3.1 Thermal expansion coefficient

Thermal expansion coefficient describes the material's response to temperate change. This response might be in its size, volume, area or length and it is computed from volume and temperature average data by fitting in this work. More explicitly, the thermal expansion coefficient depends on how volume changes as temperature changes. I have used NPT ensemble under constant pressure. The calculated the thermal expansion coefficients along with the reference to experimental thermal expansion coefficient values are listed in Table 7. The α_p is the thermal expansion coefficient, V_0 is the initial volume of the system at constant pressure and T is temperature.

$$k = \alpha_p = \frac{1}{V_0} \left(\frac{\partial V}{\partial T} \right)_p \qquad (47)$$

This second order volume energy equation gives additional information in particular for α_p' which is the derivative of thermal expansion coefficient. This equation is solved by nonlinear least square fitting method.

$$V = V_0 \left(1 + \alpha_p (T - T_0) + \frac{1}{2} \alpha_p' (T - T_0)^2 \right) \qquad (48)$$

Table 7: The calculations of thermal expansion coefficients of NiAl alloys in the single crystals and bicrystals in MD.

$\alpha 10^{-6}/K$	TEC	$\alpha 10^{-6}/K$	TEC
NiAl B2	32.1	B2Σ 3 (210)	31.4
Ni$_3$Al	53	B2Σ 5 (310)	32
NiAl$_3$	55	B2Σ 5 (210)	32
NiAl$_3$ R L12	68	A1Σ 3 (210)	12.5
NiAl L10	50	A1Σ 5 (310)	45.4
Ni$_3$Al RL12	66.1	A1Σ 5 (210)	45.4
NiAl B1	45		

The coefficient of thermal expansion is obtained from the slope of volume vs. temperature graphics and shown in Table 7. The thermal expansion coefficient values are close to each other for almost all structures but the B2 NiAl structure.

Table 8: The first order thermal expansion coefficient values with different hydrogen percentages for the NiAl single crystals.

$\alpha 10^{-9}/K^2$	0%H	1%H	2%H	5%H	8%H	10%H
NiAl B2	16.97	18.64	20.73	28.89	95.16	121.88
NiAl B1	52.61	7.98	48.74	52.19	51.60	55.35
Ni$_3$Al	8.48	8.03	7.63	6.73	6.84	7.06
NiAl$_3$	263.30	264.34	356.57	342.74	201.12	163.89
NiAl$_3$ R L12	168.59	182.71	184.16	169.86	130.27	61.06
Ni$_3$Al RL12	-5.58	1.50	3.24	8.93	13.20	16.54
NiAl L10	5.90	5.71	5.65	6.03	6.52	6.87

The first order of thermal expansion coefficient values obtained from the equation (44) that is really important for the more absolute values at higher temperature to determine.
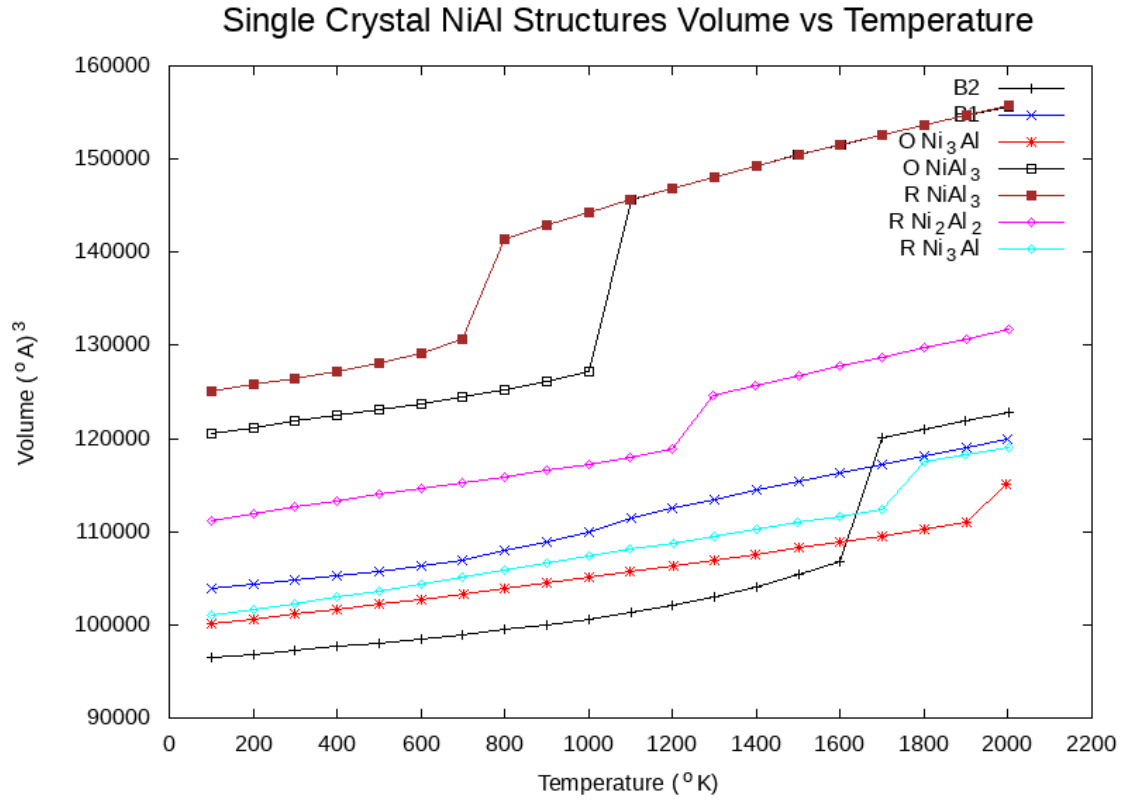
Figure 9: The volumetric change from the heating up simulations is collected for the NiAl single crystal structures at constant pressure.

The figure of the thermal expansion coefficient (TEC) of the structures also show the melting points where the line has a sharp increase starting. The B2 NiAl structure has the lowest volume at the starting point however it has a significant melting point. Also, the random alloys have higher melting points from the ordered ones. Moreover, the random NiAl$_3$ has the highest TEC and the B2 NiAl structure has the lowest TEC which does show a clear relation between them which is inversely proportional to one another.
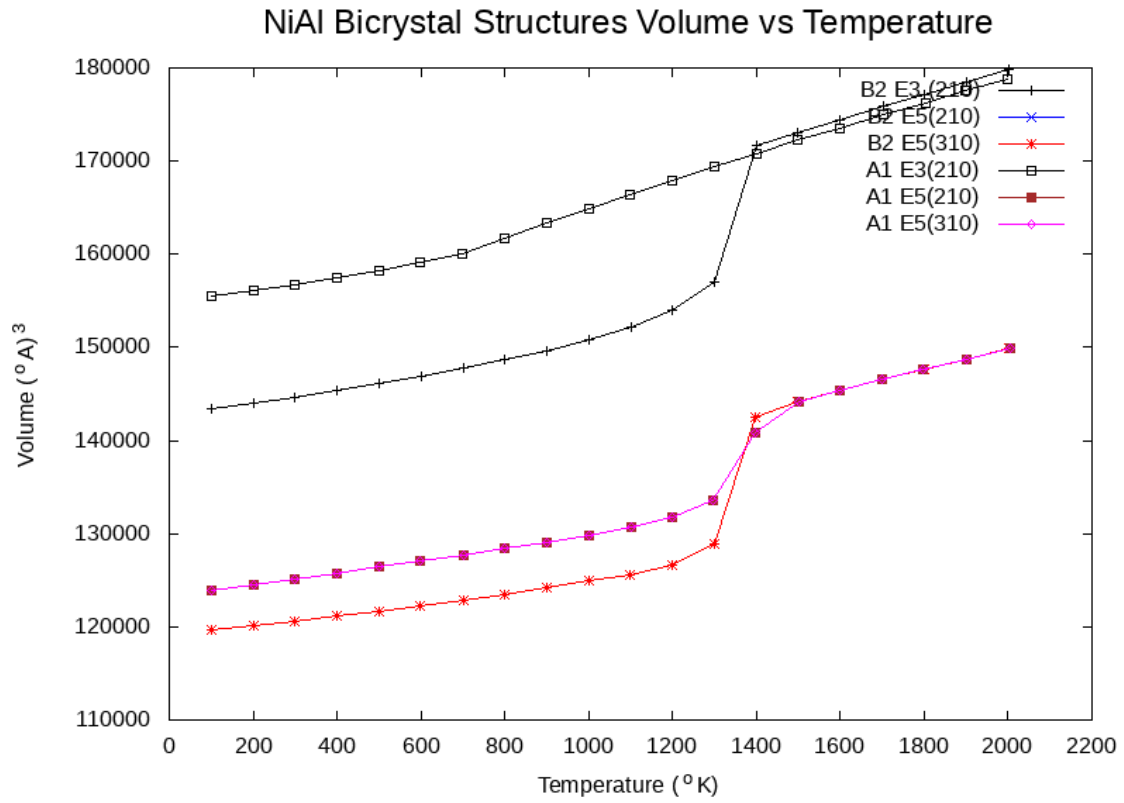
Figure 10: The bicrystals structures for thermal expansion coefficient in heating up simulations at constant pressure.

The grain boundary structures have the same trend for the thermal expansion coefficients and have the melting points that are close to each other except the A1 $\Sigma 3$ structure which does not show a clear melting point and also showing the lowest thermal expansion coefficient while the B2 structures tend to exhibit clear similar thermal expansion coefficients.

3.3.2 Isobaric specific heat capacity

I have obtained the specific heat from heating simulations which I performed in the NPT ensemble at constant pressure by conducting simulations at temperatures in increments of 100 K. After obtaining time series for volume for each temperature, I have computed the averages of them and created a temperature vs. energy curve. By fitting to the second order polynomial determined the specific heat and its temperature derivative, therefore the variation of specific heat as a function of temperature as well.

C_p is the specific heat, N is the number of atoms in the system, E is the energy and T is temperature under constant pressure.

$$C_p = \frac{1}{N}\left(\frac{\partial E}{\partial T}\right)_p \tag{49}$$

Second order equation of specific heat, in which C_p' is the derivative of the specific heat and E_0 is the initial energy.

$$E = E_0 + C_p(T - T_0) + \frac{1}{2}C_p'(T - T_0)^2 \tag{50}$$

The coefficients in this second order equation are obtained by fitting to data below the melting temperature. The coefficients in the equation are obtained by fitting the equation to data.

Table 9: The specific heat from heating up simulations for single crystal and bicrystal systems.

Structures	$J \, mol^{-1}K^{-1}$	Structures	$J \, mol^{-1}K^{-1}$
NiAl B2	24.19	L10Σ 5 (210)	24.249
NiAl B1	28.381	L10Σ 5 (310)	24.249
Ni_3Al	24.962	L10Σ 3 (210)	16.81
$NiAl_3$ R L12	25.65	B2Σ 5 (210)	24.268
NiAl L10	30.2	B2Σ 5 (310)	24.268
$NiAl_3$	24.391	B2Σ 3 (210)	23.32
Ni_3Al RL12	25.431		

The heat capacity of the single crystal structure systems is generally slightly bigger than the same structure of the bicrystals systems. The B1 NiAl and L10 NiAl have the higher values than the others and the L10Σ 3 (210) structure is the lowest.

Table 10: The specific heat values as function of hydrogen content for different single crystal models.

Structure	0%H	1%H	2%H	5%H	8%H	10%H
NiAl B2	0.000222	0.001105	0.000245	0.000271	0.000367	0.000735
NiAl B1	0.000936	0.000334	0.00092	0.000977	0.000999	0.001027
Ni_3Al	0.000159	0.000166	0.000176	0.000225	0.000317	0.000383
$NiAl_3$	0.001709	0.001661	0.002096	0.001778	0.001337	0.001481
$NiAl_3$ R L12	0.001083	0.001244	0.001279	0.001306	0.001048	0.000659
Ni_3Al RL12	0.000176	0.000223	0.000258	0.000391	0.000483	0.000557
NiAl L10	0.000166	0.000201	0.000241	0.000337	0.000472	0.000535

The derivative of the specific heat obtained from the equation (50) is actually important for more absolute values at higher temperature to determine the specific heat.

Single Crystal NiAl Structure Total Energy vs Temperature
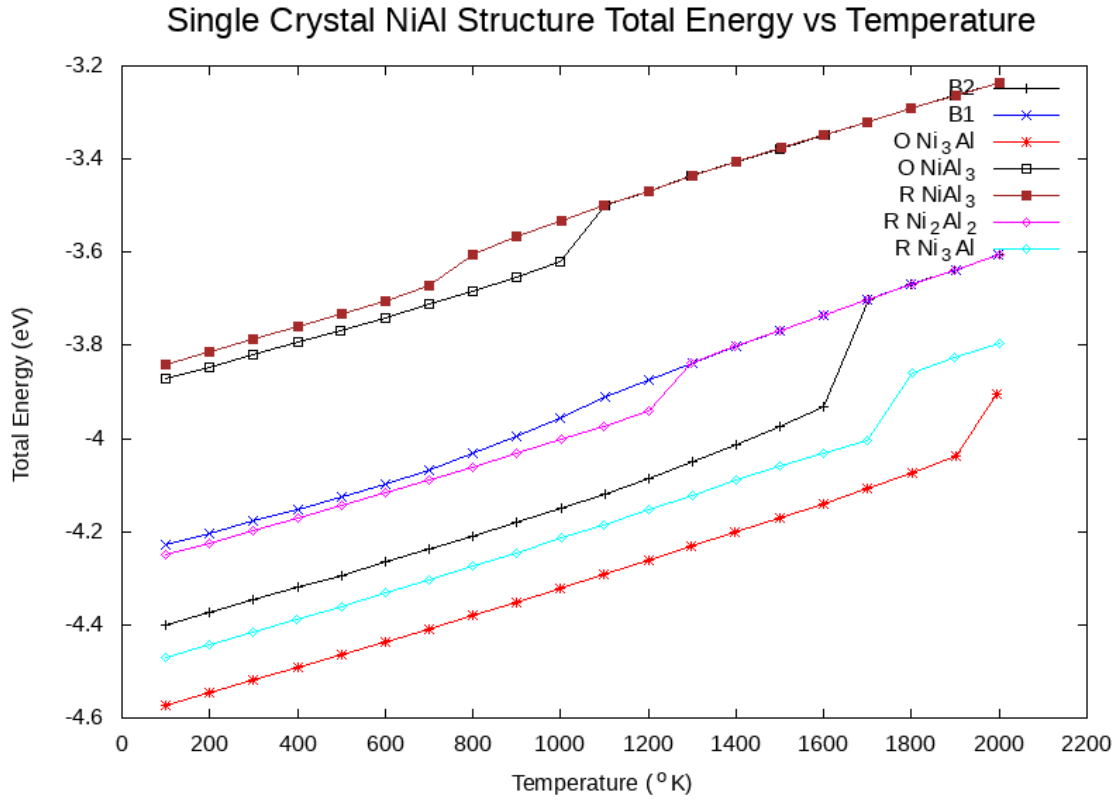
Figure 11: The isobaric specific heat from the heating up simulations for single crystal structures.

The specific heat is obtained from heating up simulations by averaging trajectory files and the total energy is obtained by dividing the number of atoms. Lastly, the slope of the total energy and temperature is gave the specific heat values. The ordered Ni$_3$Al has the highest the melting point but does not have the heist specific heat, contrarily the B1 NiAl has the highest specific heat.

NiAl Bicrystal Structures Total Energy vs Temperature
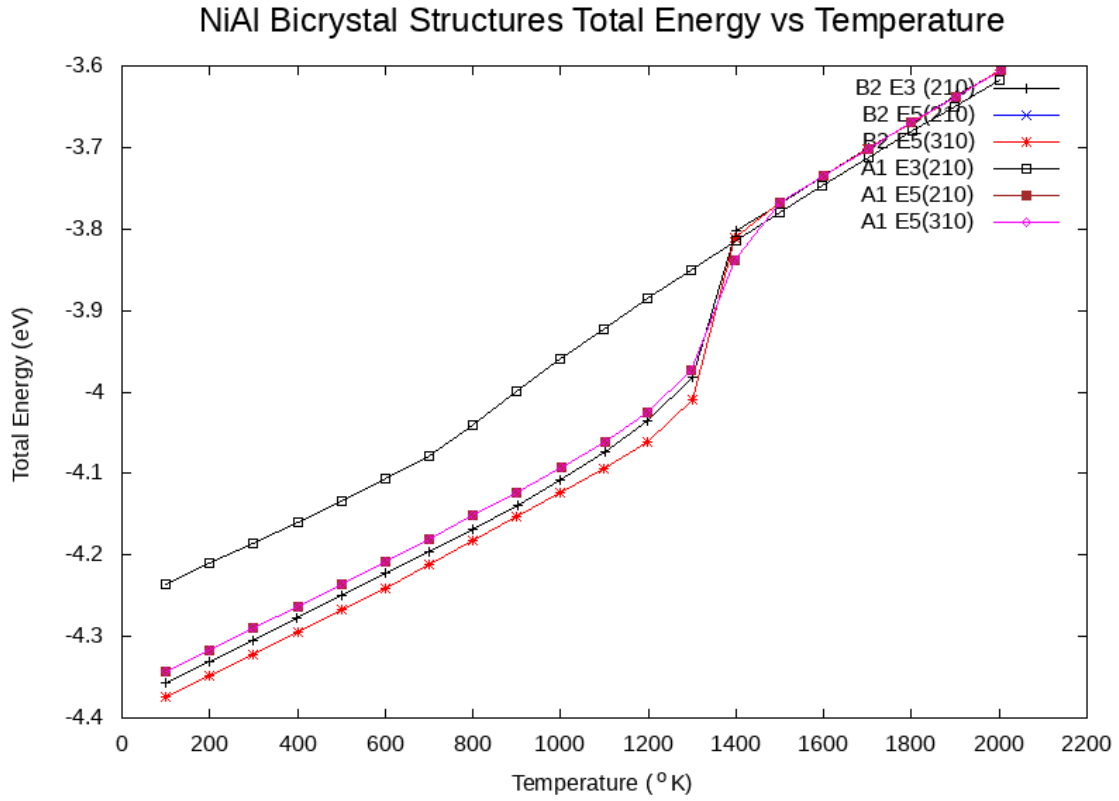
Figure 12: For bicrystal systems, the isobaric specific heat systems come from the heating simulations.

The specific heat of bicrystals systems also close to each other except L10Σ 3 (210) structure due to the direction of the grain boundary which result in a smaller specific heat. The same sigma Σ with different planes have the same specific heat values in both B2 NiAl and L10 NiAl structures which did not show a clear difference.

3.3.3 Grain boundary formation energy

The grain boundary formation energy is the energy difference between the single crystal system and the bicrystal system per area. The minimum energy in the single crystal is divided by the number of atoms in itself and then multiplied by the number of atoms in the bicrystal system. A bicrystal system has two grain boundary surface areas which is x component and y component of the 3d coordinates system. The grain boundary is built in -z direction which has 2 equal sides. The formulation is shown below;

$$E_{gf} = \left(\frac{N_g x E_n}{N_n} - E_g \right) \frac{1}{2(GBS)} \qquad (51)$$

E_{gf} is grain boundary formation energy, E_g is grain boundary minimum energy, E_n is the single crystal minimum energy, N_g is the number of grain boundary atoms, N_n is the number of atoms in single crystal, GBS is the grain boundary surface area. The grain boundary formation energy is shown in Table 11.

Table 11: The results of grain boundary formation energy of the single crystal and bicrystal in MD.

Structure	(eV/A^2) GB formation Energy
L10Σ 5 (210)	0.164672
L10Σ 5 (310)	0.164672

4. HYDROGEN EFFECT ON NIAL

The hydrogen content may have adverse influence on materials' mechanical properties. Hydrogen effect hardly displays ductility in failure mechanism before materials crack. In most new technology applications, they can encounter with hydrogen almost in all the processes therefore it is vital to comprehend the hydrogen affects in failure mechanism [49]. For instance hydrogen embrittlement phenomena has been explained through a few different mechanism systems such as hydrogen enhanced decohesion mechanism, hydrogen enhanced localized plasticity etc. [49]. The hydrogen enhanced decohesion mechanism proposes the presence of hydrogen weakens the bonding among neighboring planes in the structure which might lead the crystal structure to undergo failure processes that might create some cracks or breaks in the crystal. Those defects are perfectly places that may keep hydrogen in there. The other mechanism, hydrogen enhanced localized plasticity, suggests that the plastic behaviors start to come up with the presence of hydrogen. The enhanced plastic behaviors bring new loads with itself for the system. These loads might undergo failure process easier than the undoped hydrogen crystal systems. This system can act as a smoother surface which can move dislocations more straightforwardly than a system without hydrogen. The failure mechanism can also undergo in places which grain boundaries and dislocations overlap.

In this computational work, I have doped hydrogen at the level of 0.01, 0.02, 0.05, 0.08 and 0.1 into the crystal structures I have built which are the ordered B1, ordered B2

random L10, random and ordered L12 supercells. I have observed how hydrogen affects the systems at different amounts of hydrogen. The contribution of hydrogen to bulk modulus, the specific heat and the thermal expansion coefficient, compression and tension has been studied to observe how it has changed the thermo-mechanical properties of the structures with the different doping amounts of hydrogen. The change in bulk modulus of different crystal structures with doping hydrogen is investigated in the following structures.

4.1   The hydrogen effect on bulk modulus of NiAl

The hydrogen is doped through 1% to 10% at the temperatures of 100 ^{o}K, 300 ^{o}K, 500 ^{o}K and 700 ^{o}K in all the structures built in MD. The complications and effects of the doped H is tabled and graphed.

4.1.1 Random Ni_3Al L_{12} structure

The random L12 structure has been constructed under NPT ensemble from 0.1 GPa to 5 GPa at 100 ^{o}K, 300 ^{o}K, 500 ^{o}K and 700 ^{o}K .These temperature values were taken from the heating simulations of the end of relaxation. The system has a 13x13x13 supercell and totally 8788 atoms without any hydrogen and I doped hydrogen at the rate of 0.01, 0.02, 0.05, 0.08 and 0.1 and applied the stress afterwards observed the change of volume and pressure. It is shown in Table 12.

Table 12: The bulk modulus of hydrogen doped in GPa of the random L12 NiAl alloy at 100 K, 300 K, 500 K and 700 K temperatures in MD.

Temp.	0%H	1% H	2%H	5%H	8%H	10%H
100	153.1922	153.1279	153.0967	149.5472	150.8903	150.3289
300	135.7242	135.3563	134.7287	132.0654	131.4706	130.078
500	124.3389	123.5434	121.7323	121.3459	121.5307	120.9088
700	121.7783	119.5497	114.4262	114.3369	114.2606	112.7661

A is seen in Table 12 the bulk modules for random Ni_3Al has slightly decreased when hydrogen is doped at 1%, 2% however at 5% H, it decreased and the bulk modulus also decreased more at 8% and 10% at 100 °K. When the temperature is increased as 300 °K, 500 °K and 700 °K the bulk modulus has dropped by a little decrement of the previous change as expected. At 700, when hydrogen is doped the bulk modules slightly decreased. The volume pressure of Random Ni_3Al with different hydrogen doping at 100 °K, 300 °K, 500 °K and 700 °K of temperatures has been shown in the following figures.
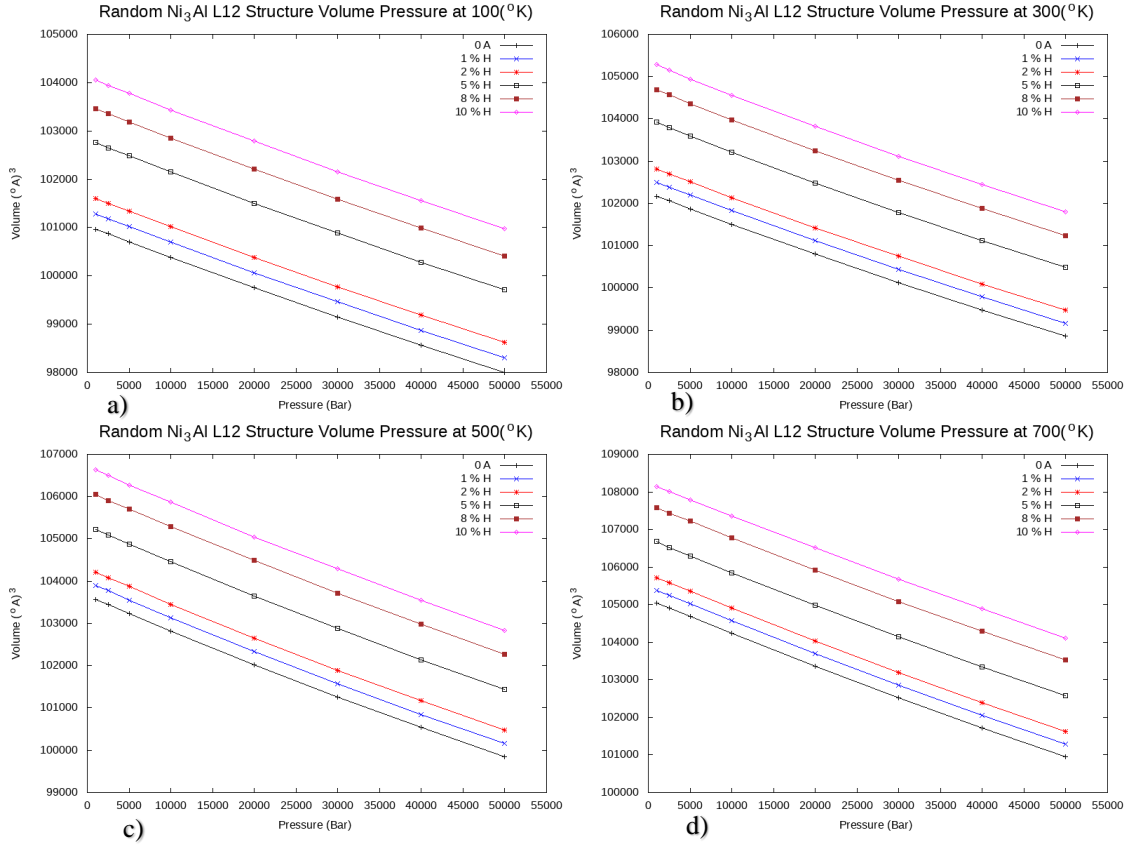
Figure 13: The hydrostatic pressure on random L12 NiAl with 0.00, 0.01, 0.02, 0.05, 0.08, 0.1 amounts of hydrogen from MD at a) 100 K, b) 300 K, c) 500 K and d) 700 K.

4.1.2 Random Ni_2Al_2 L_{10} structure

I constructed the random Ni_2Al_2 L_{10} structure with npt ensemble and I used the same pressure values as the others to apply which starts from 0.1 GPa and ends in 5 GPa. Afterwards, hydrogen atoms are doped at the rates of 0.01 0.02 0.05 0.08 0.1. The supercell I created is 13x13x13 and has 8788 atoms at the beginning at 100 ^{o}K, 300 ^{o}K, 500 ^{o}K and 700 ^{o}K temperatures.

Table 13: The bulk modulus of hydrogen doped in GPa of the L10 NiAl alloy at 100 K, 300 K, 500 K and 700 K temperatures in MD.

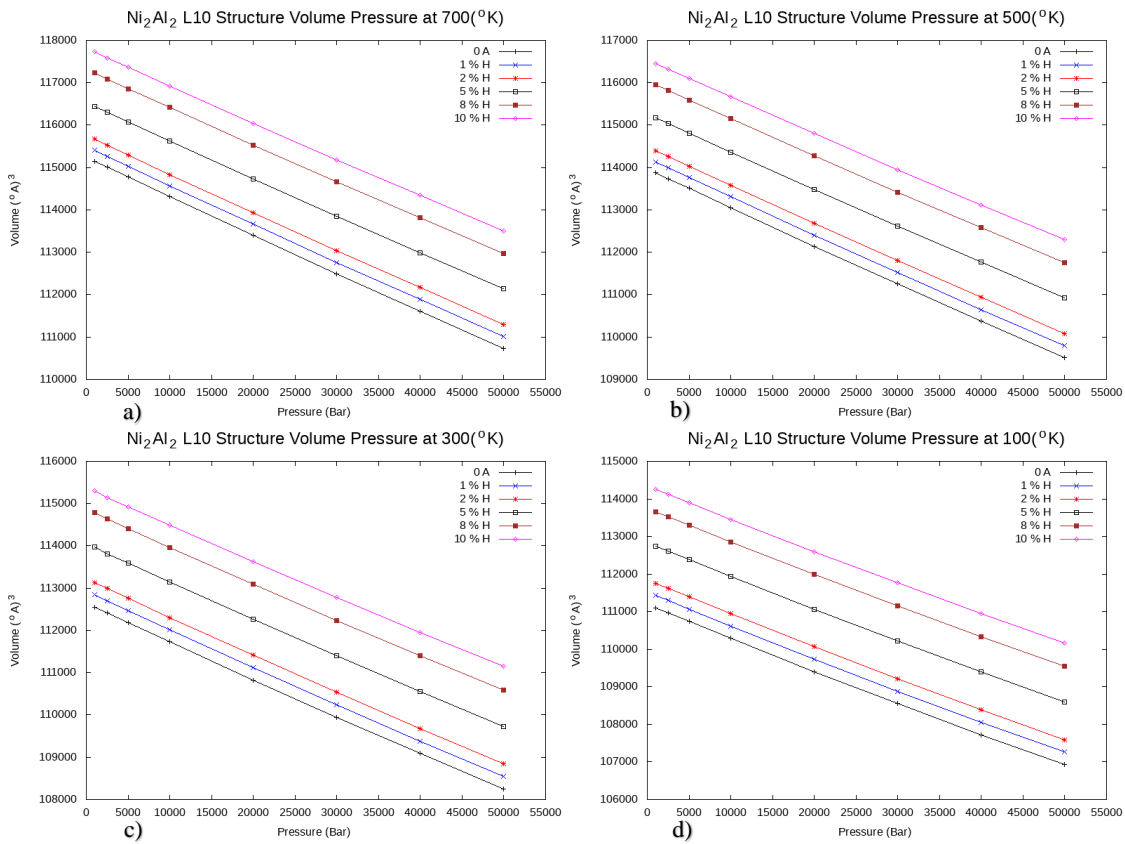| Temperature	0%H	1%H	2%H	5%H	8%H	10%H
100	130.715	129.636	127.190	124.567	123.803	122.693
300	132.043	128.881	127.090	124.829	123.943	122.942
500	129.227	126.739	124.494	122.365	121.718	121.200
700	127.938	126.843	123.652	121.489	120.570	119.942

Figure 14: The bulk modulus of the random L10 NiAl structure under hydrostatic pressure with 0.00, 0.01, 0.02, 0.05, 0.08, 0.1 amounts of hydrogen from MD at a) 100 K, b) 300 K, c) 500 K and d) 700 K.

Random Ni_2Al_2 bulk modulus decreased as hydrogen doped regularly. The doping hydrogen in the random Ni_2Al_2 affected the bulk modulus more than the random Ni_3Al.

The volume and pressure change of the random L_{10} Ni_2Al_2 is shown at 100 °K, 300 °K, 500 °K and 700 °K temperatures in the following figures.

4.1.3 Random $NiAl_3$ structure

I have built bulk modulus system with isotropic conditions and the NPT ensemble which begins from 0.1 GPa to 5 GPa at 100 °K, 300 °K, 500 °K and 700 °K in which temperatures taken from the heating simulations at the end of the relaxation of the same temperature. I have built a supercell which has 13x13x13 unit cell and totally 8788 atoms. The volume and pressure change obtained from the average data for the hydrogen rates of 0.01, 0.02, 0.05, 0.08 and 0.1. The simulation results is shown in.

Table 14: The bulk modulus of the random L12 AlNi alloy at 100 K, 300 K, 500 K and 700 K in MD.

Temperature	0%H	1%H	2%H	5%H	8%H	10%H
100	118	105	98	96	87	82
300	110	98	96	89	81	64
500	96	93	91	81	66	49
700	71	71	72	49	47	43

In the figure 12 random $NiAl_3$ bulk modulus has decreased as hydrogen doped respectively. The bulk modulus has some fluctuations at 500 °K which is irregular according to the previous and later temperature and is affected more than random $NiAl_3$. The volume and pressure change of the random $NiAl_3$ is shown at 100 °K, 300 °K, 500 °K and 700 °K in the following figures;
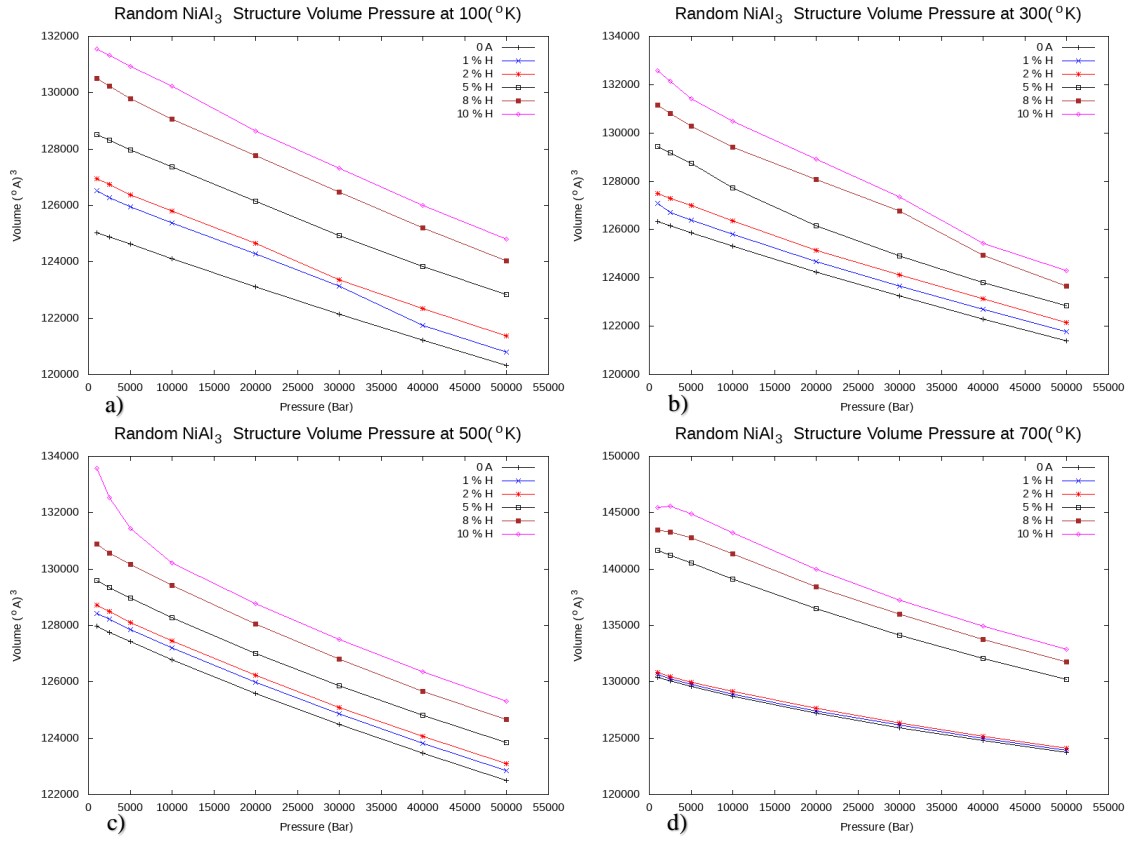
Figure 15: The volume change obtained under the hydrostatic pressure for bulk modulus of the random L12 AlNi structure with 0.00, 0.01, 0.02, 0.05, 0.08, 0.1 amounts of hydrogen from MD at a) 100 K, b) 300 K, c) 500 K and d) 700 K.

4.1.4 B1 NiAl structure

The bulk modulus system with isotropic conditions and the NPT ensemble in lammps was built by starting the pressure from 0.1 GPa to 5 GPa at 100 °K, 300 °K, 500 °K and 700 °K and the temperature values gotten from the heating simulations at the end of the relaxation of that temperature. A supercell which has 10x10x10 unit cells total 8000 atoms has been built. The volume pressure change curve for the hydrogen rates of 0.01, 0.02, 0.05, 0.08 and 0.1 have been tabled and the simulation results are shown.

Table 15: After doping hydrogen, the bulk modulus of the B1 NiAl alloy at 100 K, 300 K, 500 K and 700 K in MD.

Temperature	0%H	1%H	2%H	5%H	8%H	10%H
100	139	138	137	135	135	135
300	132	129	125	126	133	130
500	126	120	122	125	117	124
700	105	91	90	81	74	59

The bulk modulus with the hydrogen doping has gone down somewhat and affected slightly and almost did not often affect it however at 100 ^{o}K, it has changed more than the others , especially at 700 ^{o}K it has decreased very sharply in comparison to others. The volume and pressure change of the random B1 NiAl structure is shown at 100 ^{o}K, 300 ^{o}K, 500 ^{o}K and 700 ^{o}K in the following figures.

Figure 16: From the increasing pressure simulations, bulk modulus of the B1 NiAl structure with 0.00, 0.01, 0.02, 0.05, 0.08, 0.1 amounts of hydrogen from MD at a) 100 K, b) 300 K, c) 500 K and d) 700 K.

4.1.5 B2 NiAl structure

I have constructed bulk modulus system with isotropic conditions and the NPT ensemble in lammps starting from 0.1 GPa to 5 GPa at 100 ^{o}K, 300 ^{o}K, 500 ^{o}K and 700 ^{o}K in which temperatures taken from the heating simulations at the end of the relaxation of that temperature. I have built a supercell which has 16x16x16 unit cells total 8192 atoms. I have had the volume- pressure change curve plotted from the average data for the hydrogen rates of 0.01, 0.02, 0.05, 0.08 and 0.1.

Table 16: The B2 NiAl structure with doping hydrogen , the bulk modulus obtained at 100 K, 300 K, 500 K and 700 K in MD.

Temp	0%H(GPa)	1%H(GPa)	2%H(GPa)	5%H(GPa)	8%H(GPa)	10%H(GPa)
100	185.9053	185.402	184.2654	183.286	182.844	182.4805
300	176.3902	176.713	176.0447	175.7542	175.8515	175.5541
500	167.1696	167.1221	166.5062	166.2009	163.9045	162.4221
700	165.4386	156.8212	155.5651	154.1888	151.3823	124.9213

As is seen, the bulk modulus has its highest value at 100 ^{o}K with 10% hydrogen as doping H at 100 ^{o}K has decreased bulk modulus in other words it has become weakened however, as temperature increased the bulk modulus generally decreased. The bulk modulus decreases with increasing temperature as expected 1% hydrogen almost did not affect the system and only has a very small margin effect. 2% has more influence on the system but still cannot be thought it is effective. After 5% percent doped H, it shows its effect more and cannot be ignored anymore. Lastly, the 10% hydrogen doped system shows its effect at 700 ^{o}K most therefore it decreased bulk modulus almost 25% which can cause failure in there more probably than the other systems. The change in bulk modules doped 1%, 2%, 5%, 8% and, 10% H has shown at 100 ^{o}K, 300 ^{o}K, 500 ^{o}K 700 ^{o}K.
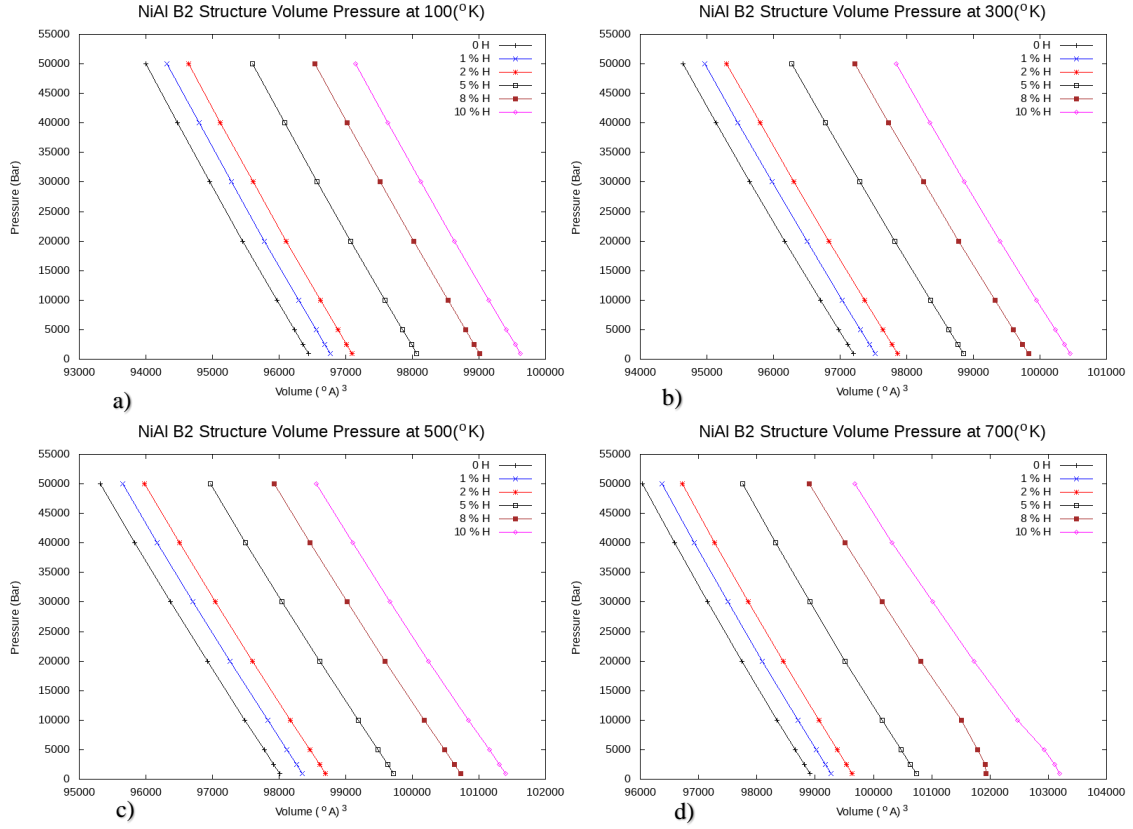
Figure 17: The bulk modulus of the B2 NiAl structure obtained from the hydrostatic pressure with 0.00, 0.01, 0.02, 0.05, 0.08, 0.1 amounts of hydrogen from MD at a) 100 K, b) 300 K, c) 500 K and d) 700 K.

4.1.6 Ordered Ni_3Al L_{12} structure

The nickel aluminum L12 structure, that is Ni_3Al, that has three nickel atoms and one aluminum atom in one unit cell was built. I expanded thirteen times in each direction and having total 8788 atoms. I doped hydrogen to the system at different percentages that are 1%, 2%, 5%, 8% and, 10% with NPT ensemble under isotropic conditions applying pressure from 0.1 GPa to 5 GPa at four different temperature which are 100 °K, 300 °K,

61

500 °K 700 °K in which temperatures obtained from the heating up simulations at the

last part of the relaxation of that temperature.

Table 17: The bulk modulus of the ordered L12 NiAl structure with doping hydrogen collected at 100 K, 300 K, 500 K and 700 K in MD.

Temp	0% H(GPa)	1% H(GPa)	2% H(GPa)	5% H(GPa)	8% H(GPa)	10%H(GPa)
100	179.106	179.598	177.542	173.476	172.557	171.676
300	161.095	160.495	159.918	159.310	159.957	158.248
500	151.142	150.718	148.000	147.014	147.677	146.366
700	144.628	143.285	141.654	139.479	139.132	138.662

The highest bulk modulus value is at 100 °K with 10% H doping. This indicates that

adding hydrogen weakened the system while increasing temperature decreased bulk

modulus as expected. %1 H and 2% H doping affected the system in very small

amounts. The 5% H, 8% H and 10% H doping changed bulk modulus with reasonable

amounts. Moreover, it has lowest value at 700 °K without H doping.
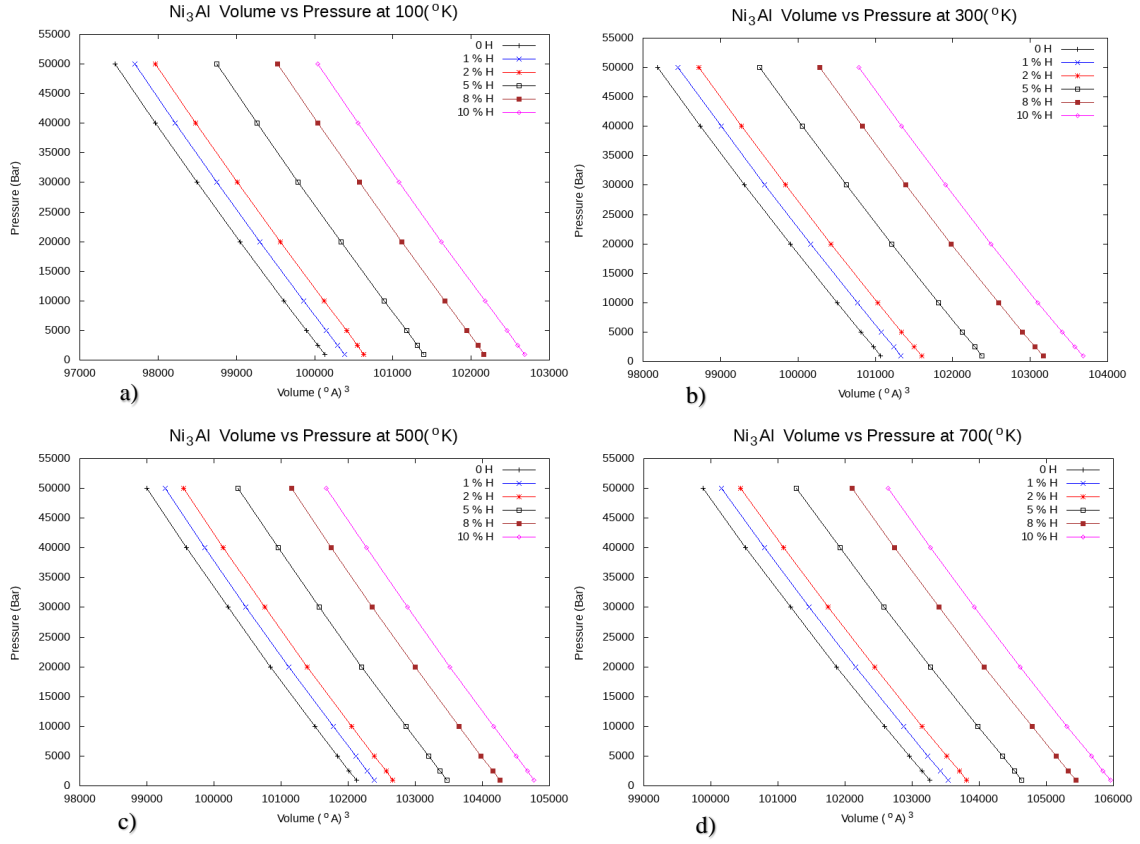
Figure 18: The hydrostatic pressure tests give the bulk modulus of the ordered L12 NiAl structure obtained with 0.00, 0.01, 0.02, 0.05, 0.08, 0.1 amounts of hydrogen from MD at a) 100 K, b) 300 K, c) 500 K and d) 700 K.

4.1.7 Ordered NiAl$_3$ structure

The NiAl$_3$ has three aluminum atoms and one nickel atom in L12 structure I created a 13x13x13 supercell and total 8788 atoms doping amounts that are the same as others structure that I have built are 1%, 2%, 5%, 8% and, 10%. The same tendency observed when the data investigated.

63

Table 18: The bulk modulus of the ordered L12 AlNi structure with doping hydrogen collected at 100 K, 300 K, 500 K and 700 K in MD.

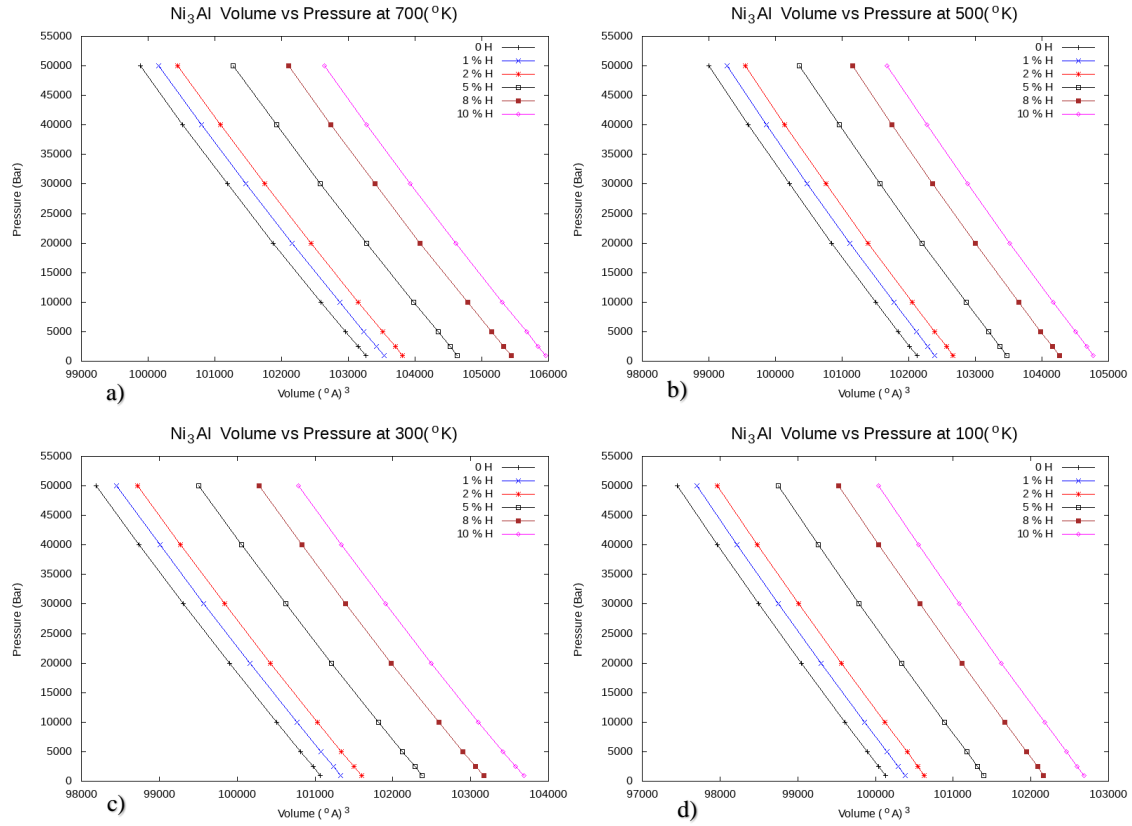| Temp	0% H(GPa)	1% H(GPa)	2% H(GPa)	5% H(GPa)	8% H(GPa)	10% H(GPa)
100	179.7849	155.317	151.1193	149.1629	148.3219	147.5059
300	160.7499	152.0467	148.2053	148.8992	148.7644	148.3096
500	212.3647	152.9055	143.8452	142.124	142.9068	138.2981
700	145.7897	133.1246	131.4177	129.8997	121.7505	70.29901

Figure 19: The bulk modulus of the ordered L12 AlNi obtained from the hydrostatic pressure with 0.00, 0.01, 0.02, 0.05, 0.08, 0.1 amounts of hydrogen from MD at a) 100 K, b) 300 K, c) 500 K and d) 700 K.

H increased the embrittlement of the system due to the decreased bulk modulus.

It has highest value at 10%H doped at 100 °K and then it starts to decrease at higher temperatures as is seen in other structures. However there is different observation at 8 percentages of 500 °K it suddenly increased and then suddenly went down to the lowest value. This can have happened due to instability Ni-Al L12 system.

4.2   The hydrogen effect of the specific heats on NiAl alloys

Specific heats of samples are obtained for H-content levels ranging from 1%, 2%, 5%, 8% and, 10% H using NPT ensemble in MD simulations from 100 °K to 2000 °K. The results are tabulated in Table 15.

Table 19: The specific heat of NiAl alloy with the doped hydrogen values in MD.

Doping of H	NiAl B2 $j \, mol^{-1} K^{-}$	Ni_3Al L12 $j \, mol^{-1} K^{-}$	$NiAl_3$ $j \, mol^{-1} K^{-}$	$NiAl_3$ RL12 $j \, mol^{-1} K^{-}$	NiAl L10 $j \, mol^{-1} K^{-}$	Ni_3Al RL12 $j \, mol^{-1} K^{-}$	NiAl B1 $j \, mol^{-1} K^{-}$
0%	24.81	24.50	30.96	27.65	24.39	25.42	28.61
1%	23.66	24.68	30.58	27.04	24.41	25.52	28.50
2%	23.48	24.28	29.85	27.08	23.69	24.90	28.17
5%	23.79	23.51	29.69	26.68	23.19	24.31	27.87
8%	23.97	23.15	29.95	26.32	23.35	24.15	26.99
10%	23.27	23.24	28.56	26.18	23.28	24.24	25.15

By doping hydrogen we changed the specific heat value of the materials. The b2 NiAl3 Random Ni2Al2 structure affected slightly other structures have changed more in comparison. The Ni3Al structure has a sharp decrease at 2 % and 5% and then it goes up sharply again in other structure these changes is less significant.
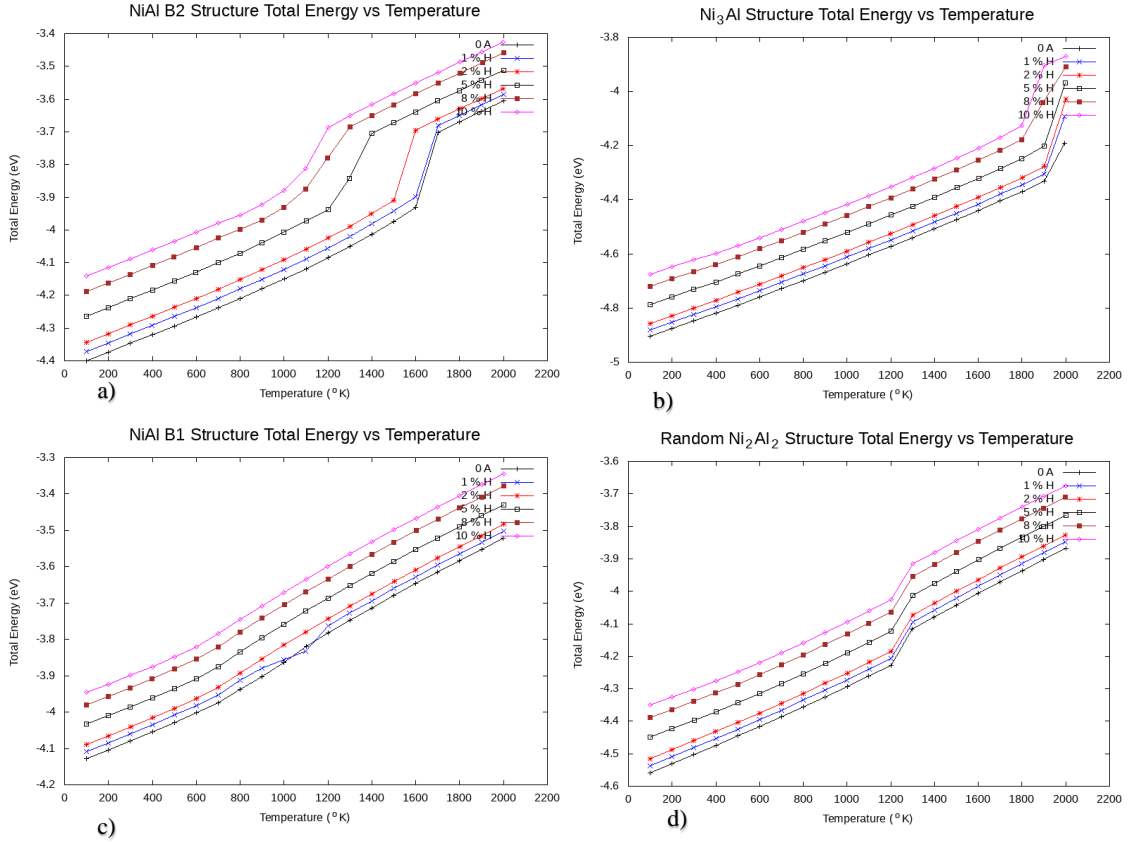
Figure 20: The isobaric specific heat from the heating up simulations is collected for the at constant pressure, with 0.00, 0.01, 0.02, 0.05, 0.08, 0.10 amounts of hydrogen in ordered L12 NiAl, B1 NiAl, B2 NiAl and L10 NiAl alloys.

4.3   The hydrogen effect of the thermal expansion coefficient on NiAl

Thermal expansion coefficients are obtained for hydrogen content levels ranging from 1%, 2%, 5%, 8% and, 10% H which is using NPT ensemble in MD simulations from 0 $^{\circ}$K to 2100 $^{\circ}$K with the increment of 100 $^{\circ}$K. The initial structures which were constructed as regular heating up simulations. The hydrogen occupied the interstitial sites that were randomly chosen until it took up the 10% of the whole system. After doping hydrogen the volumetric change and temperature difference were collected. This

66

procedure repeated for the whole amounts and the data collected from the trajectories

and were averaged. Consequently, the results are tabulated in Table 16.

Table 20: Thermal expansion coefficient of NiAl alloys with hydrogen in MD.

$\alpha 10^{-6}/K$	NiAl B2	Ni_3Al L12	$NiAl_3$ R L12	NiAl L10	Ni_3Al RL12	NiAl B1	$NiAl_3$ L12
0%	32.1	53	68	50	66.1	45	55
1%	34.5	53.5	72	50.6	66.2	48	55.5
2%	36.7	54	76	51	66.6	53	56
5%	40.2	55	81	52.2	66.7	61	58
8%	44.7	57	86	53	66.8	70	62
10%	48.9	58	90	54	67.7	80	67

The hydrogen amounts heavily affected the thermal expansion coefficient of almost

all the structures. The hydrogen decreased the melting point of the structures as seen in

the figures. This effect is expected due to the inverse proportionality of melting point

and thermal expansion coefficient.
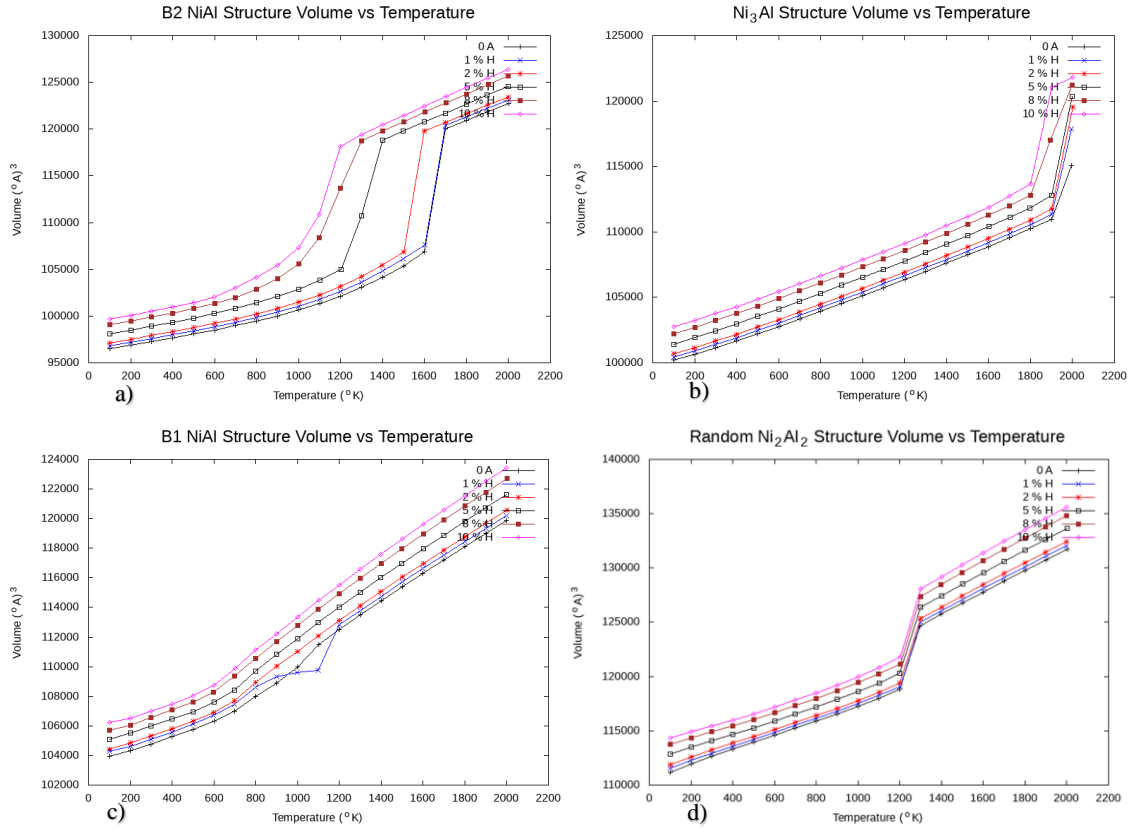
Figure 21: The thermal expansion with 0.00, 0.01, 0.02, 0.05, 0.08, 0.10 amounts of hydrogen in a) B2 NiAl, b) ordered L12 NiAl c) B1 NiAl and d) random L10 NiAl

4.4   The hydrogen effect of uniaxial tests on NiAl

In single crystal, I have employed compressive uniaxial load test in x direction applying stress ranging from 0.1 GPa to % 5GPa under NPT ensemble at 100 K, 300 K , 500K and 700K s by with hydrogen concentrations in the system set to 1%, 2%, 5%, 8% and, 10%.
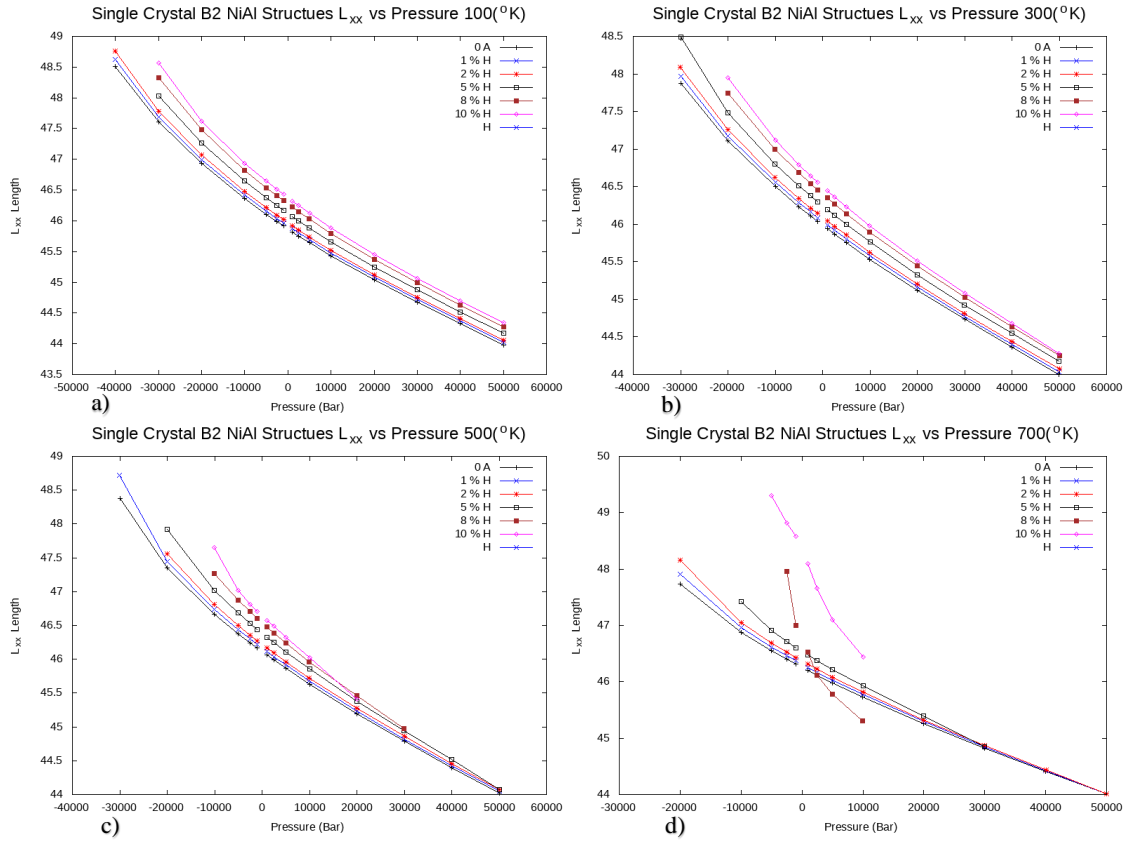
Figure 22: The compression-tension test of the B2 NiAl with 0.00, 0.01, 0.02, 0.05, 0.08, 0.10 amounts of H gives the young modulus at a) 100 K, b) 300 K, c) 500 K and d) 700 K.

The uniaxial tests were applied on the x direction and the change on x direction was noted as hydrogen doped until 10% percentages. The initial structures obtained from the heating up simulations for constant temperature. Therefore, the uniaxial pressure applied on opposite direction of x axis. Further, the pressure applied from 0 GPa to 5 GPa. The slope of the L_x and the P_x gave the young modulus and hydrogen decreased the slope at 700 °K extensively after 5 % of H. Consequently, the same behavior observed on the other structures.

69

5. CONCLUSIONS

I have investigated elastic constants of NiAl structures that are B1, B2, L10, L12, L10 and A4 along with pure Al and pure Ni in dft for using the Vasp code. First off, I have checked elastic stability conditions for these structures and B1 and A4 NiAl structures failed to suffice these conditions. Both structures cannot stand under shear stress. The metastability conditions have not been satisfied for A4 structure of NiAl and B1 structure of NiAl which means the difference of C_{11} and C_{12} and C44 values have negative values which is not possible for a stable structure. The other structures have satisfied the stability conditions as expected B2 and L12 crystal structures of NiAl and pure Ni are found the most stable structures due to the delta energy that means the energy difference of the structure and that of the pure Ni and Al proportions. Meanwhile, I have employed MD simulations to compare thermo-mechanical properties with single crystal and bicrystal systems. I have compared bulk modulus, heat capacity thermal expansion coefficient and I also have calculated grain boundary formation energy of B1 and L10 structures for Σ 5(210), Σ 5(310), Σ 3(310) misorientations with the (210) and (310) planes. The grain boundary energy has very little changed on the different planes of the same structures.

Afterwards, the doped hydrogen to the systems was investigated of hydrogen effect. When doping hydrogen I observed that the bulk modulus has totally decreased the stability of the structures due to the decrease in bulk modulus, young modulus and increase in thermal expansion coefficient. On specific heat it has slightly decreased the

heat capacity. The thermal expansion coefficient has been affected on various manners that have many fluctuations but generally decreased when hydrogen is doped. The compression and tensile stresses have changed very considerably by doping hydrogen at higher temperatures. At higher temperatures, hydrogen affects the structures more heavily.

The ordered NiAl structures have higher melting points than that of the random NiAl structures. The derivative of the isobaric specific heat and thermal expansion coefficient obtained which give the values of themselves at higher temperatures. The initial structures of hydrostatic pressure and uniaxial pressure obtained from heating up simulations which show the fluctuation effects as well. The bicrystal structures with grain boundaries are less strong than the same structures with the single crystal systems.

REFERENCES

1.   Switendick, A., *Hydrogen in Metals I: Basic Properties, edited by G. Alefeld and J. Volkl*. 1978, Springer, Berlin.

2.   Wert, C., *Trapping of hydrogen in metals.* Hydrogen in Metals II, 1978: p. 305-330.

3.   Korzhavyi, P.A., et al., *Constitutional and thermal point defects in B 2 NiAl.* Physical Review B, 2000. 61(9): p. 6003.

4.   Fukai, Y., *The metal-hydrogen system: basic bulk properties*. Vol. 21. 2006: Springer Science & Business Media.

5.   Hanh, T.T.T., Y. Takimoto, and O. Sugino, *First-principles thermodynamic description of hydrogen electroadsorption on the Pt (111) surface.* Surface Science, 2014. 625: p. 104-111.

6.   Vykhodets, V., et al. *Diffusion of Light Elements in BCC, FCC and HCP Metals*. in *Solid State Phenomena*. 2008. Trans Tech Publ.

7.   Johnson, W.H., *On some remarkable changes produced in iron and steel by the action of hydrogen and acids.* Nature, 1875. 11(281): p. 393.

8.   Ganchenkova, M., V.A. BOrodin, and R.M. Nieminen, *Hydrogen in beryllium: Solubility, transport, and trapping.* Physical Review B, 2009. 79(13): p. 134101.

9.   Jacob, T. and W.A. Goddard, *Adsorption of atomic H and O on the (111) surface of Pt3Ni alloys.* The Journal of Physical Chemistry B, 2004. 108(24): p. 8311-8323.

10.   Huda, M. and A. Ray, *A density functional study of atomic hydrogen adsorption on plutonium layers.* Physica B: Condensed Matter, 2004. 352(1): p. 5-17.

11.   Moody, N., et al., *Atomistic simulation of the hydrogen-induced fracture process in an iron-based superalloy*. 1995, Sandia National Labs., Livermore, CA (United States).

12.   Eliaz, N., D. Fuks, and D. Eliezer, *Non-Arrhenius behavior of the diffusion coefficient of hydrogen in amorphous metals.* Materials Letters, 1999. 39(5): p. 255-259.

13.   Hsieh, C. and W. Tuan, *Thermal expansion behavior of a model ceramic–metal composite.* Materials Science and Engineering: A, 2007. 460: p. 453-458.

14.   Stöckel, D., *The shape memory effect-phenomenon, alloys and applications.* California, 1995. 94539: p. 1-13.

15.   Smith, W., *Elements of Molecular Dynamics*. January 2014.

16.   Lazar, P. and R. Podloucky, *Ab initio study of tension-shear coupling in NiAl.* Physical Review B, 2007. 75(2): p. 024112.

17.   Li, T., J. Morris Jr, and D. Chrzan, *Ab initio study of the ideal shear strength and elastic deformation behaviors of B2 FeAl and NiAl.* Physical Review B, 2006. 73(2): p. 024105.

18.   George, E., et al., *Characterization, processing, and alloy design of NiAl-based shape memory alloys.* Materials Characterization, 1994. 32(3): p. 139-160.

19.   Soykan, C., et al., *Ab initio calculations of martensitic phase behavior in Ni 2 FeGa magnetic shape memory alloys.* Journal of Alloys and Compounds, 2014. 611: p. 225-234.

20.   Momma, K. and F. Izumi, *VESTA 3 for three-dimensional visualization of crystal, volumetric and morphology data.* Journal of Applied Crystallography, 2011. 44(6): p. 1272-1276.

21.   Kresse, G. and J. Furthmüller, *Efficiency of ab-initio total energy calculations for metals and semiconductors using a plane-wave basis set.* Computational Materials Science, 1996. 6(1): p. 15-50.

22.   Kresse, G. and J. Furthmüller, *Efficient iterative schemes for ab initio total-energy calculations using a plane-wave basis set.* Physical review B, 1996. 54(16): p. 11169.

23.   Kresse, G. and J. Hafner, *Ab initio molecular dynamics for liquid metals.* Physical Review B, 1993. 47(1): p. 558.

24.   Kresse, G. and D. Joubert, *From ultrasoft pseudopotentials to the projector augmented-wave method.* Physical Review B, 1999. 59(3): p. 1758.

25.   Kresse, G. and J. Hafner, *Norm-conserving and ultrasoft pseudopotentials for first-row and transition elements.* Journal of Physics: Condensed Matter, 1994. 6(40): p. 8245.

26. Frankel, J., et al., *The elastic constants of Ni3Al to 1.4 GPa.* Physica B+ C, 1986. 139: p. 198-201.

27. Wang, Y., Z.-K. Liu, and L.-Q. Chen, *Thermodynamic properties of Al, Ni, NiAl, and Ni 3 Al from first-principles calculations.* Acta Materialia, 2004. 52(9): p. 2665-2671.

28. Fu, C. and M. Yoo. *Stacking fault energies, crystal elasticity and their relation to the mechanical properties of L1 2-ordered alloys*. in *MRS Proceedings*. 1988. Cambridge Univ Press.

29. Hill, R., *The elastic behaviour of a crystalline aggregate.* Proceedings of the Physical Society. Section A, 1952. 65(5): p. 349.

30. Ponomareva, A., et al., *Site preference and effect of alloying on elastic properties of ternary B 2 NiAl-based alloys.* Physical Review B, 2012. 85(14): p. 144117.

31. Chen, G.-X., J.-M. Zhang, and K.-W. Xu, *Self-diffusion of Ni in B2 type intermetallic compound NiAl.* Journal of alloys and compounds, 2007. 430(1): p. 102-106.

32. Papanicolaou, N., et al., *Second-moment interatomic potential for Al, Ni and Ni– Al alloys, and molecular dynamics application.* Computational materials science, 2003. 27(1): p. 191-198.

33. Mehl, M.J., B.M. Klein, and D.A. Papaconstantopoulos, *First-principles calculation of elastic properties of metals*. Vol. 1. 1994: Wiley, London.

34. Chuan-Hui, Z., et al., *Chen's lattice inversion embedded-atom method for Ni—Al alloy.* Chinese Physics B, 2012. 21(11): p. 113401.

35. Fu, H., et al., *Ab initio calculations of elastic constants and thermodynamic properties of NiAl under high pressures.* Computational Materials Science, 2008. 44(2): p. 774-778.

36. Gross, E. and R. Dreizler, *Density functional theory: an approach to the quantum many-body problem*. 1990, Springer, Berlin.

37. Harrison, N., *An introduction to density functional theory.* NATO SCIENCE SERIES SUB SERIES III COMPUTER AND SYSTEMS SCIENCES, 2003. 187: p. 45-70.

38. Capelle, K., *A bird's-eye view of density-functional theory.* arXiv preprint cond-mat/0211443, 2002.

39.   Sham, L. and M. Schlüter, *Density-functional theory of the energy gap.* Physical Review Letters, 1983. 51(20): p. 1888.

40.   Jones, R.O., *Density functional theory: Its origins, rise to prominence, and future.* Reviews of modern physics, 2015. 87(3): p. 897.

41.   Burke, K., *The abc of dft.* Department of Chemistry, University of California, 2007.

42.   Kohn, W., A.D. Becke, and R.G. Parr, *Density functional theory of electronic structure.* The Journal of Physical Chemistry, 1996. 100(31): p. 12974-12980.

43.   Orio, M., D.A. Pantazis, and F. Neese, *Density functional theory.* Photosynthesis research, 2009. 102(2-3): p. 443-453.

44.   Pople, J.A., P.M. Gill, and B.G. Johnson, *Kohn—Sham density-functional theory within a finite basis set.* Chemical physics letters, 1992. 199(6): p. 557-560.

45.   Kresse, G. and J. Hafner, *Ab initio molecular-dynamics simulation of the liquid-metal–amorphous-semiconductor transition in germanium.* Physical Review B, 1994. 49(20): p. 14251.

46.   Oh, D. and R. Johnson, *Simple embedded atom method model for fec and hcp metals.* Journal of Materials Research, 1988. 3(03): p. 471-478.

47.   Yao, H., L. Ouyang, and W.Y. Ching, *Ab initio calculation of elastic constants of ceramic crystals.* Journal of the American Ceramic Society, 2007. 90(10): p. 3194-3204.

48.   *Unit Conversions*. Available from: http://greif.geo.berkeley.edu/~driver/conversions.html.

49.   Angelo, J.E., N.R. Moody, and M.I. Baskes, *Trapping of hydrogen to lattice defects in nickel.* Modelling and Simulation in Materials Science and Engineering, 1995. 3(3): p. 289.